

**EXPERIMENTAL INVESTIGATION OF TURBULENT  
STRUCTURES AND NON-EQUILIBRIUM EFFECTS IN  
AXIAL WAKE VORTICES VIA PARTICLE IMAGE  
VELOCIMETRY**

by

Jeffry William Ely  
Bachelor of Science in Mechanical Engineering

A Thesis Submitted to the Faculty of  
Old Dominion University in Partial Fulfillment of the  
Requirements for the Degree of

MASTER OF SCIENCE

AEROSPACE ENGINEERING

OLD DOMINION UNIVERSITY  
May 2016

Approved by:

---

Robert Ash (Director)

---

Drew Landman (Member)

---

Colin Britcher (Member)

## ABSTRACT

### EXPERIMENTAL INVESTIGATION OF TURBULENT STRUCTURES AND NON-EQUILIBRIUM EFFECTS IN AXIAL WAKE VORTICES VIA PARTICLE IMAGE VELOCIMETRY

Jeffry William Ely  
Old Dominion University, 2016  
Director: Dr. Robert Ash

Vortices are a common phenomenon in fluid flows that arise to dissipate kinetic energy into heat via viscous interaction. They arise naturally at large scales in the form of dust devils, tornadoes, and in the wake of aircraft. It is important to understand the conditions leading to their formation, their duration, and their dissipation to prevent undesirable effects. Among these effects is a decrease in safety of aircraft operations in the wake of other aircraft, an extremely common situation at airports around the world. A large number of mathematical models and experimental data exists to help explain various aspects of axial wake vortex behavior, but current models fail to understand why many vortices remain tightly wound about their cores for as long as they have been observed to do. The current study builds upon the theoretical work of Ash, Zardadkhan and Zuckerwar [?], and tests specific attributes of a vortex for agreement with non-equilibrium pressure relaxation theory. A bi-wing vortex generator was constructed, and placed in a low speed wind tunnel. Stereo particle image velocimetry was employed to map three dimensional velocity vectors in a plane perpendicular to the free stream flow direction at a rate of 1Hz for 200 seconds. A Reynolds time averaging approach was used to synthesize this velocity data into stable and fluctuating components. Free stream velocity and downstream distance were varied to create a variety of vortices, and to ensure the availability of high quality data.

Copyright, 2016, by Jeffry William Ely, All Rights Reserved.

**NOTES**

## TABLE OF CONTENTS

	Page
LIST OF TABLES .....	vi
LIST OF FIGURES .....	vii
Chapter	
1. INTRODUCTION .....	1
1.1 FUNDAMENTALS OF PARTICLE IMAGE VELOCIMETRY .....	2
2. EXPERIMENT SETUP .....	5
2.1 LOW SPEED WIND TUNNEL .....	7
2.2 VORTEX GENERATOR .....	8
2.3 PIV OVERVIEW .....	11
2.4 STEREO PIV DATA ACQUISITION .....	20
2.5 STEREO PIV DATA PROCESSING .....	33
2.6 UNCERTAINTY IN PIV MEASUREMENTS .....	47
3. EXPERIMENT RESULTS .....	52
BIBLIOGRAPHY .....	53
APPENDICES	
VITA .....	54

## LIST OF TABLES

Table	Page
1 Experimental conditions for all 70 experiments .....	6
2 Pixel displacements by up sampling order. ....	19
3 Experimental measurements for station 1 .....	30
4 Experimental measurements for station 2 .....	31
5 Experimental measurements for station 3 .....	31
6 Experimental measurements for station 4 .....	32
7 Experimental measurements for station 5 .....	32
8 Experimental measurements for station 6 .....	33
9 Experimental measurements for station 7 .....	33
10 Example rows from v3d files with raw 3d vector data .....	34

## LIST OF FIGURES

Figure	Page
1 Velocity vector field of a vortical flow structure as produced by PIV. ....	2
2 ODU Low speed wind tunnel. ....	7
3 Schematic diagram of systems under wind tunnel PC control. ....	8
4 Picture of the vortex generator set up in the ODU LSWT. ....	10
5 CAD design of the vortex generator used in this study. ....	11
6 Single camera PIV system for mapping two dimensional velocity vectors .	13
7 Stereo camera PIV system for mapping three dimensional velocity vectors	13
8 Colorized 32x32 pixel contour images at $t = 0$ (left), and $t = dt$ (right), no up sampling. ....	17
9 Overlaid sector snapshots (left) and corresponding correlation map (right), no up sampling. ....	17
10 Colorized 32x32 pixel contour images at $t = 0$ (left), and $t = dt$ (right), 6th order up sampling. ....	18
11 Overlaid sector snapshots (left) and corresponding correlation map (right), 6th order up sampling. ....	18
12 Top view schematic of PIV camera positions. A-vortex generator, B-PIV calibration target and interrogation plane, C-left camera, D-right camera, E-station distance dimension. ....	21
13 Picture of a light curtain illuminating a cross section of an axial wake vortex. ....	22
14 Frame straddling technique. Laser pulses are shown in green, and camera exposures are shown in gray. ....	23
15 Blockdiagram of PIV hardware components. C-left camera, D-right camera, F-Nd:YAG laser, G-laser control unit and power supply, H- synchronizer, J-control PC running INSIGHT software suite. ....	24
16 Inverted color and elevated contrast photograph of the calibration target, highlighting the central fiducial mark. ....	25

17	Example stream plot.	40
18	Example contour plot of $\bar{u}$ .	40
19	Example contour plot of $\bar{v}$ .	41
20	Example contour plot of $\bar{w}$ .	41
21	Example contour plot of $\bar{r}$ .	42
22	Example contour plot of $\bar{t}$ .	42
23	Example contour plot of $\bar{r}'t'$ .	43
24	Example contour plot of $\bar{r}'w'$ .	43
25	Example contour plot of $\bar{t}'w'$ .	44
26	Example contour plot of $\bar{r}'r'$ .	44
27	Example contour plot of $\bar{t}'t'$ .	45
28	Example contour plot of $\bar{w}'w'$ .	45
29	Example contour plot of turbulent kinetic energy $k$ .	46
30	Example scatter plot of $T$ , colored by $k$ .	46
31	Example contour plot showing the variation in the number of measurements within the interrogation plane	47

## Chapter 1

### INTRODUCTION

## 1.1 FUNDAMENTALS OF PARTICLE IMAGE VELOCIMETRY

Particle Image Velocimetry, or PIV, is a class of methods employed by experimental fluid mechanics to measure instantaneous vector velocity fields by measuring the displacements of small visible particles which follow the motion of the fluid [?]. Figure 1 shows a typical resulting vector field from measurements of a vortical flow. Each of these two-dimensional vectors was measured simultaneously in a thin sheet of fluid. The velocity of the fluid is sensed by acquiring images of well entrained particles at precise times and measuring the displacement of those particles. This is accomplished with the use of cameras for acquiring images and an intense laser to illuminate particles within the desired plane. This technique can be used to study flows in gases and liquids, and is derived from techniques originally developed to measure deformations on the surface of solid material.

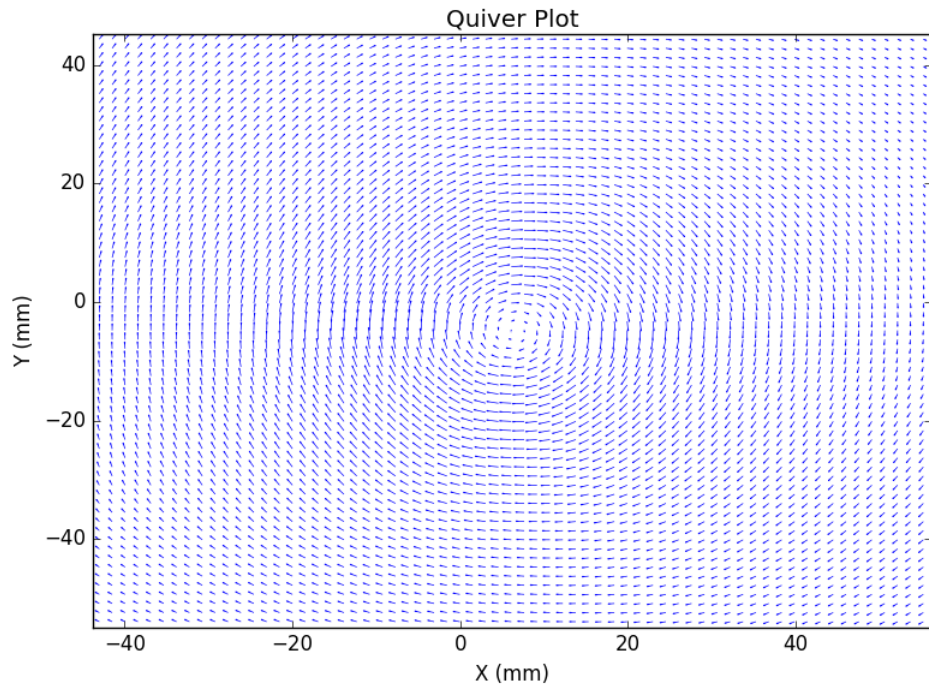


**Figure 1:** Velocity vector field of a vortical flow structure as produced by PIV.

### 1.1.1 THE CASE FOR PIV

Unlike other flow measurement techniques, PIV is a non-invasive method to directly measure time and displacement, and thus velocity. PIV is also capable of

resolving vector measurements at many positions within a two dimensional slice of the flow field simultaneously, while other measurement techniques require taking data at many locations sequentially over a much greater period of time. Single camera PIV can measure two components of the velocity vectors aligned with the image plane, but the PIV method is capable of resolving many dimensions of fluid flow with incremental increases in system complexity. The addition of another camera allows the full three dimensional velocity vector to be measured, and a sweeping beam laser allows the interrogation of an entire volume of flow field instead of a slice.

Stereo PIV is used widely because it provides a full velocity vector, and requires only an additional camera, slightly more complex calibration and software to process the imagery. A stereo PIV system with a stationary sheet laser can resolve three dimensional velocity vectors and their fluctuations within a two dimensional slice of fluid flow. A two point correlation tensor containing important information about the turbulent structure of a flow can be obtained readily with PIV. The non-invasive nature of PIV, combined with the ability to interrogate a flow volume very quickly for information with high dimensionality makes it exceptionally useful in fluid mechanics. [?]

### **1.1.2 PRINCIPLES OF PLANAR PIV**

A simple planar PIV system consists of a double pulsed laser, light sheet forming optics, particle seed, a single lens camera, image digitization hardware, and a computer system for data storage and subsequent analysis. The underlying concept behind all PIV is that light scattered from the particles as they move through the flow field allows a pair of images to capture information about the motion of that particle. Double pulsed illumination is commonly used in PIV systems due to its relatively low cost and complexity compared with multiple laser source systems. The energy required to adequately illuminate an area of interest depends upon the size of that area, and the scattering properties of the particle seed. Solid state Nd:YAG lasers are typically used for this purpose [?]. An  $(X, Y, Z)$  coordinate system is defined within the light sheet that exists in  $(X, Y)$  space, and relates linearly to a coordinate system in the image plane of the camera in  $(X_p, Y_p)$  pixel space. At a time  $t$ , a laser light sheet is produced for a short pulse and the camera captures an image of the light scattering from particles within the flow. At some short time later,  $t + dt$ , a second pulse occurs and a second image is taken. By measuring the pixel

displacements ( $\Delta X_p, \Delta Y_p$ ) for a particle in the image plane, and transforming the coordinates into the plane of the laser one obtains ( $\Delta X, \Delta Y, \Delta Z$ ). This coordinate transform can be obtained from precise information about the optical geometry of the system, or by direct measurement of calibration data [?]. The method of direct measurement of a calibration target was used in this research.

### **1.1.3 PRINCIPLES OF STEREO PIV**

#### **1.1.4 PARTICLES**

**Particle Dynamics**

**Error Due to Slip**

**Seeding Particles for PIV**

#### **1.1.5 IMAGE PROCESSING**

[?, ?].

#### **1.1.6 INTERROGATION**

#### **1.1.7 MEASUREMENT OF FLUID FLOW**

#### **1.1.8 PIV IN THREE DIMENSIONS**

#### **1.1.9 PRACTICAL PIV SYSTEMS**

## Chapter 2

### EXPERIMENT SETUP

A complete particle image velocimetry system was installed in the ODU low speed wind tunnel and employed to measure three-dimensional velocity fields produced by an axial vortex at multiple nominal velocities  $V_{nom}$  and multiple interrogation planes. The interrogation planes were defined by their distance downstream of trailing edges of the bi-wing the vortex generator  $I_Z$ . Nominal wind tunnel velocity was varied from  $15m/s$  to  $33m/s$ , sampling 10 distinct velocities in increments of  $2m/s$ . The interrogation plane was moved at irregular intervals from  $546mm$  to  $1016mm$  as shown in table 1. This chapter discuss details of the experimental setup used to produce these datasets, including wind tunnel control, vortex generator setup, PIV system calibration, data acquisition, data processing, and data quality control.

Run	$I_Z$	$V_{nom}$	Run	$I_Z$	$V_{nom}$	Run	$I_Z$	$V_{nom}$
	ID	(mm)		ID	(mm)		ID	(mm)
1	546	15	31	863	15	61	1016	15
2	546	17	32	863	17	62	1016	17
3	546	19	33	863	19	63	1016	19
4	546	21	34	863	21	64	1016	21
5	546	23	35	863	23	65	1016	23
6	546	25	36	863	25	66	1016	25
7	546	27	37	863	27	67	1016	27
8	546	29	38	863	29	68	1016	29
9	546	31	39	863	31	69	1016	31
10	546	33	40	863	33	70	1016	33
11	708	15	41	914	15			
12	708	17	42	914	17			
13	708	19	43	914	19			
14	708	21	44	914	21			
15	708	23	45	914	23			
16	708	25	46	914	25			
17	708	27	47	914	27			
18	708	29	48	914	29			
19	708	31	49	914	31			
20	708	33	50	914	33			
21	787	15	51	965	15			
22	787	17	52	965	17			
23	787	19	53	965	19			
24	787	21	54	965	21			
25	787	23	55	965	23			
26	787	25	56	965	25			
27	787	27	57	965	27			
28	787	29	58	965	29			
29	787	31	59	965	31			
30	787	33	60	965	33			

**Table 1:** Experimental conditions for all 70 experiments

## 2.1 LOW SPEED WIND TUNNEL

The Old Dominion University low speed wind tunnel (LSWT) was outfitted with a bi-wing axial vortex generator. The tunnel has a large test section measuring  $2.134m$  wide by  $2.438m$  tall and a small test section measuring  $1.219m$  wide by  $0.911m$  tall. The wind tunnel air is propelled with a frequency controlled 125 Horsepower motor. Flow velocity was manipulated directly by manually controlling voltage supplied to the controller. The small test section has a total length of  $2.438m$ , and the vortex generator spaned the  $0.911m$  height of the test section and was mounted  $0.610m$  from the front end, leaving  $1.829m$  downstream for the axial vortex to develop. The  $3 \times 4$  foot test section has a functional free stream velocity range between 12 and 55 meters per second or between 35 and 120 miles per hour.

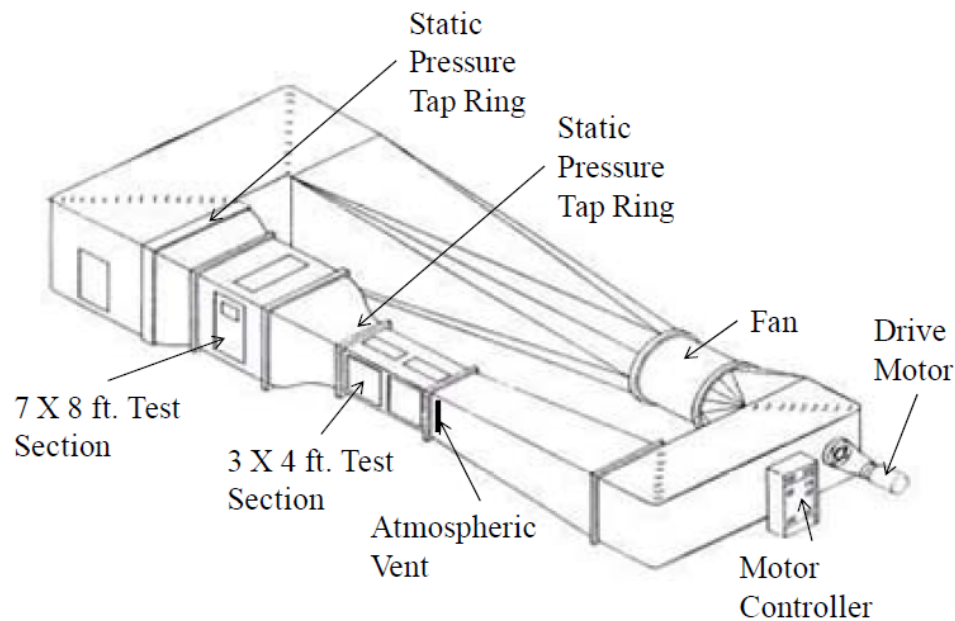


**Figure 2:** ODU Low speed wind tunnel.

The entire interior of the test section remained vacant and unobstructed with the

exception of the vortex generator. No internal traverse systems or structures were present during PIV data acquisition unless otherwise indicated. Tunnel velocity was determined by direct measurement of dynamic pressure ( $q$ ), which is monitored and controlled by the tunnel control PC. Figure 3 contains a schematic diagram of the systems under the wind tunnel control PC.

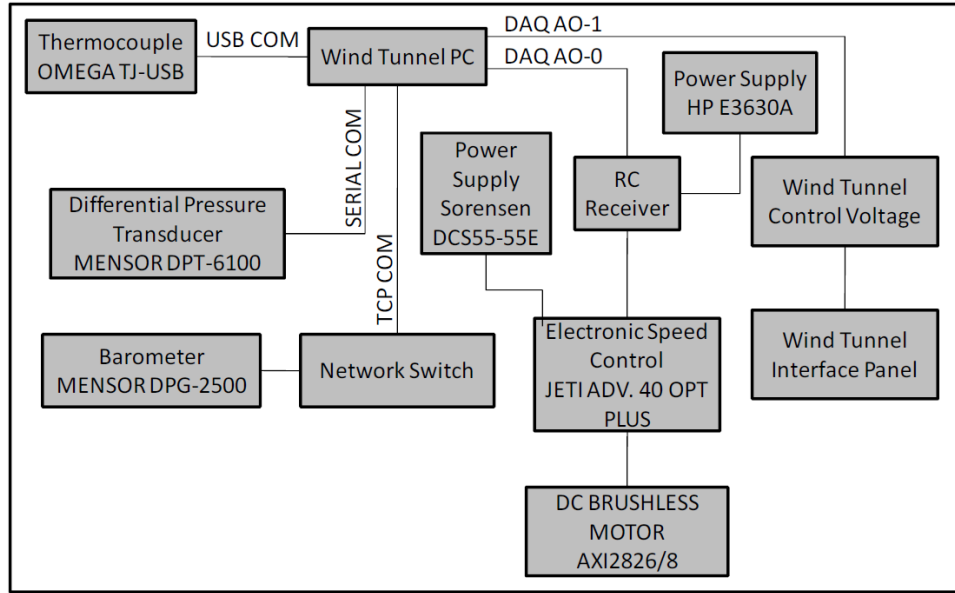


**Figure 3:** Schematic diagram of systems under wind tunnel PC control.

## 2.2 VORTEX GENERATOR

It is desirable to enhance understanding of trailing axial vortices generated by aircraft wingtips and their behavior. While naturally occurring axial vortices occur in unpredictable and non-uniform environments, this experimental investigation required that a repeatable axial vortex. Small-scale aircraft axial wake vortices can be generated in an enclosed wind tunnel environment with a single wingtip, but the downwash behavior of a wingtip vortex is distorted by the walls of the wind tunnel

and test section. A bi-wing vortex generator, as pictured in Figures 4 and 5, was designed and constructed by undergraduate student researchers to generate a vortex formed by merging two juncture vortices of opposite sign and resulting in a single vortex, absent any downwash [?]. The vortex generator employed two symmetric NACA-0012 airfoils manufactured from foam casts attached to a  $25.4\text{mm}$  diameter cylindrical center body with hemispherical forward and aft end caps. While the vortex generator could be permitted to have variable angles-of-attack, the wings were locked at an angle of attack of  $\pm 8$  degrees to avoid vortex structural distortions that could result from non-repeatable changes in angle-of-attack.



**Figure 4:** Picture of the vortex generator set up in the ODU LSWT.

ITEM NO.	PART NUMBER	DESCRIPTION	QTY.
1	Rod	Brass Rod to support wings	2
2	Wing	Naca 0012- Made with foam	2
3	Flow Aligned Cylinder	Aluminum center piece	1
4	Pin	Pins Flow Aligned Cylinder to Rod	1
5	Mounting Plate	Mounts assembly to wind tunnel	2
6	Push Pin	Pins wings angle of attack	2
7	Wing End	Naca 0012-Made of aluminum	2
8	Steel Rod	Steel Rod that runs though assembly	1
9	Keyway	Keyway used to lock steel rod	2

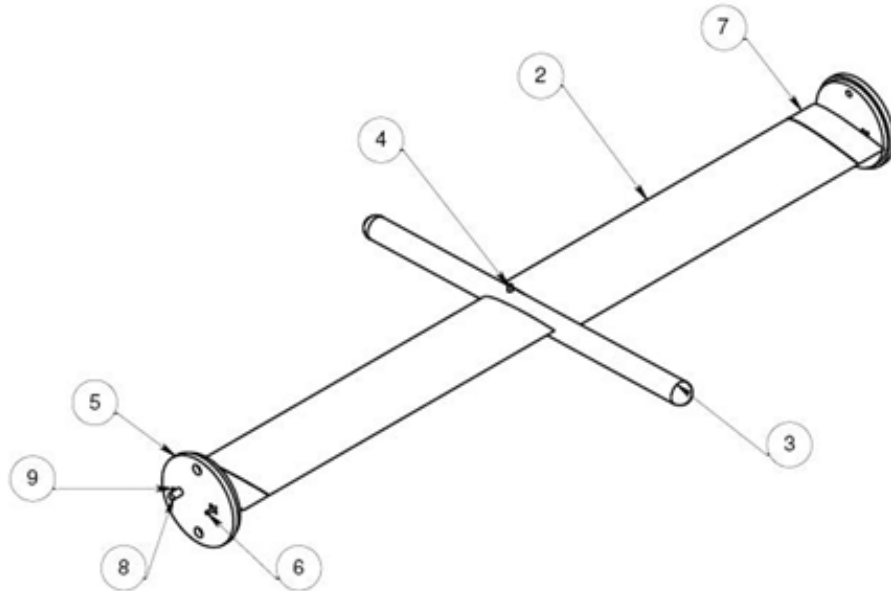


**Figure 5:** CAD design of the vortex generator used in this study

### 2.3 PIV OVERVIEW

Particle image velocimetry (PIV) is a flow measurement technique using a flow seed particulate, precisely illumination by a laser, and special cameras which take multiple closely spaced pictures of the flow. First, the fluid flow is seeded with an aerosolized oil fog, which forms tiny, low mass droplets which become well entrained in the air. A laser is broadcast into a very thin sheet which illuminates a cross section of the flow, where small inhomogeneities in the distribution of seed particles

can be seen. Cameras are positioned to take pictures of the particulate seed in rapid succession, such that the displacement of any particular particle group is just a few pixels in the image plane of the camera. By tracking movements of particle groupings through each image taken at a specific and precise moments in time, with detailed information about the geometry of optical setup, displacements in the pixel domain can be mapped into displacements in the real spatial domain. These displacements can then be translated into velocities.

Particle image velocimetry has several advantages and disadvantages over other flow measurement techniques. Firstly, PIV is non-invasive, with no solid positioning system and sensor probe to create its own wake and influence on the flow field. Secondly, PIV can make instantaneous and simultaneous measurements of an entire two dimensional surface within a flow field. This can greatly reduce uncertainty associated with single point surveys over a flow field where variation in time and space require very fine control over temperature, humidity, and free stream velocity of the flow field in order to isolate. Thirdly, PIV can be scaled to accommodate multi-dimensional requirements. One camera and laser is sufficient to measure two dimensional velocity components in a two dimensional slice of space as in figure 6. Two cameras and a laser is sufficient to measure three dimensional velocity components in a two dimensional slice of space as in figure 7. With multiple polarized laser beams, it is possible even to measure three dimensional velocity fields within a volume of space.

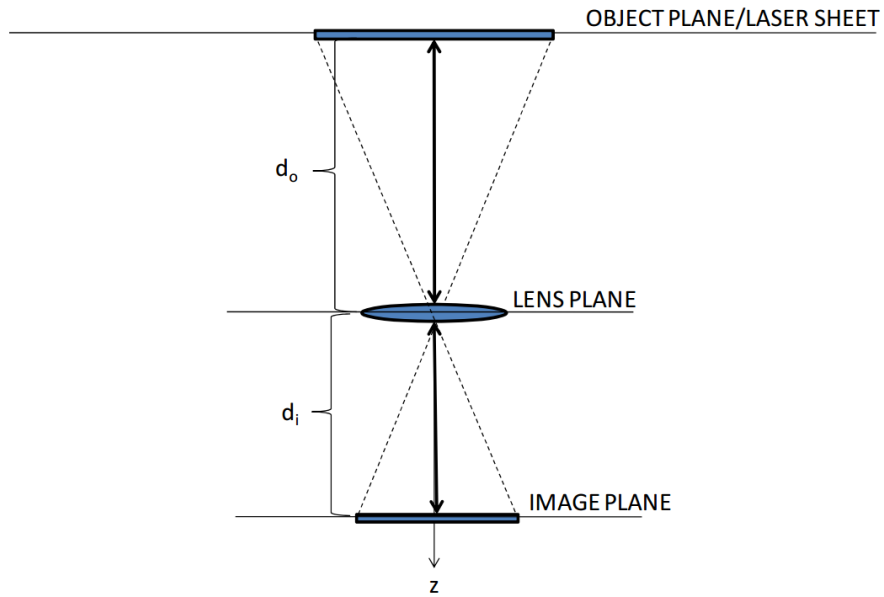


**Figure 6:** Single camera PIV system for mapping two dimensional velocity vectors

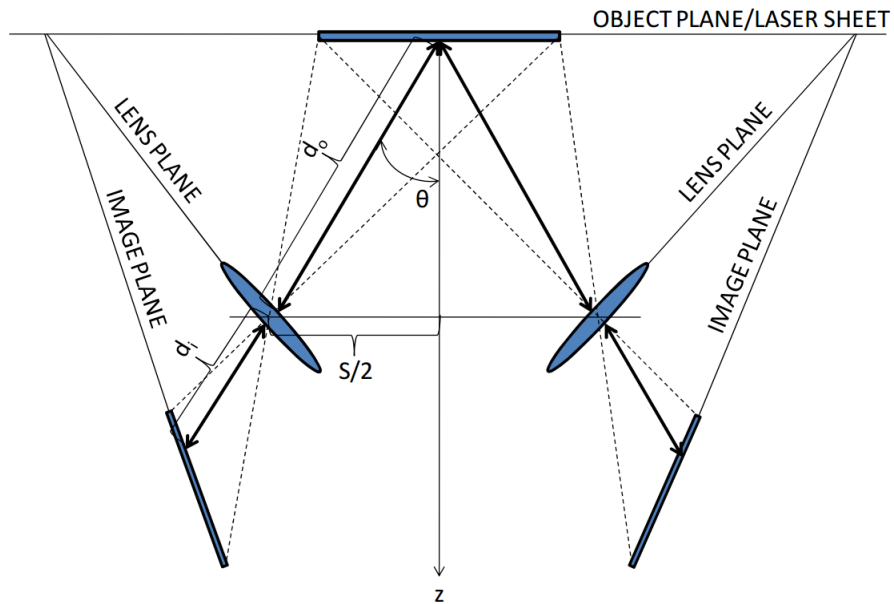


**Figure 7:** Stereo camera PIV system for mapping three dimensional velocity vectors

A significant disadvantage is that the sampling rate is restricted by the shutter speed on the cameras, and this shutter speed can easily be slower than the time

scales at which turbulent phenomena may occur. As technology improves, this disadvantage is slowly vanishing, as cameras with sampling rates on the order of 20kHz are becoming available, though at extremely high cost. An additional disadvantage which also erodes with improved computing power is the relatively high computational intensity of processing large volumes of raw image data into fully resolved vector fields, especially at a high sampling rate.

The present study uses a stereo PIV system which resolves three dimensional vectors gridded to a two dimensional cross section of flow. The cameras used are capable of taking two images a few microseconds apart, but cannot fully open and close the shutter that quickly. Deriving velocity vectors requires two images just a few microseconds apart, but pairs of images can be taken at greater time intervals. The PIV method used in this study relies upon a frame straddling technique, that times laser pulses at the edges of the camera exposures in order to meet this requirement. This results in two cameras, which simultaneously take a pair of images, and 25-50 microseconds later take a second pair of snapshots for a total of four images, Ra, Rb, La, and Lb (flag, math notation). This can be repeated once every second, resulting in a true sampling frequency of 1Hz.

### **2.3.1 MATHEMATICAL BASIS**

The mathematics behind derivation of velocity vector fields from stereo image pairs is based upon coordinate transformations from pixel coordinates to real coordinates with the following equations 1 to 4.

$$x_L = X \frac{dx_L}{dX} + Y \frac{dx_L}{dY} + Z \frac{dx_L}{dZ} \quad (1)$$

$$x_R = X \frac{dx_R}{dX} + Y \frac{dx_R}{dY} + Z \frac{dx_R}{dZ} \quad (2)$$

$$y_L = X \frac{dy_L}{dX} + Y \frac{dy_L}{dY} + Z \frac{dy_L}{dZ} \quad (3)$$

$$y_R = X \frac{dy_R}{dX} + Y \frac{dy_R}{dY} + Z \frac{dy_R}{dZ} \quad (4)$$

where  $x_L$ ,  $x_R$ ,  $y_L$  and  $y_R$  are the pixel displacements in the x direction on the left and right cameras, and the y direction on the left and right cameras respectively. Symbols  $X$ ,  $Y$ , and  $Z$  are real spatial particle displacements in the interrogation plane. The set of twelve derivatives are pixel displacement sensitivity coefficients, which are determined by a calibration process which involves taking pictures of a matrix of bright dots with a known distance between each dot. Once all twelve calibration coefficients are known, the set of equations is actually over constrained, with four equations and only three unknowns, a least squared method will be used to map measurements from the image plane to the real plane. In the case of this study, INSIGHT software was used to generate this set of calibration coefficients.

Pixel displacements are computed by significantly up sampling the images by interpolation, dividing each image into many small sectors, and comparing an image  $A$  with a image  $B$  with a correlation map. The image is up sampled to higher resolution to allow sub-pixel displacements to be measured, thus preventing accuracy

limitations associated with the physical dimensions of each pixel. The image is typically divided into grids 16 by 16 pixels in size, with 50% overlap with surrounding grids to ensure particles which started inside the sector at  $t = 0$ , but begin to exit the sector at  $t = dt$ , are still identifiable. The correlation map is computed by taking the inverse fast Fourier transform (FFT) of the product of the FFT of the first image, and the complex conjugate of the FFT of the second image, then adjusting for up-sampling by dividing by the original factor as in equation 5.

$$C_{map} = FFT^{-1} * [F_A \times conj(F_B)] \quad (5)$$

where  $C_{map}$  is the correlation map,  $F_A$  is the fast Fourier transform of image  $A$ , at time  $t = 0$  and  $F_B$  is the fast Fourier transform of image  $B$  at time  $t = dt$ .

Figure 8 shows a sample of two side by side images taken several microseconds,  $dt$  apart without any up-sampling. Figure 9 shows a sample of the same two images layered on top of each other to show the apparent horizontal displacement between the two images. The two dimensional correlation map shows a clear peak down at four pixels in the  $X$  direction and zero pixels in the  $Y$  direction.

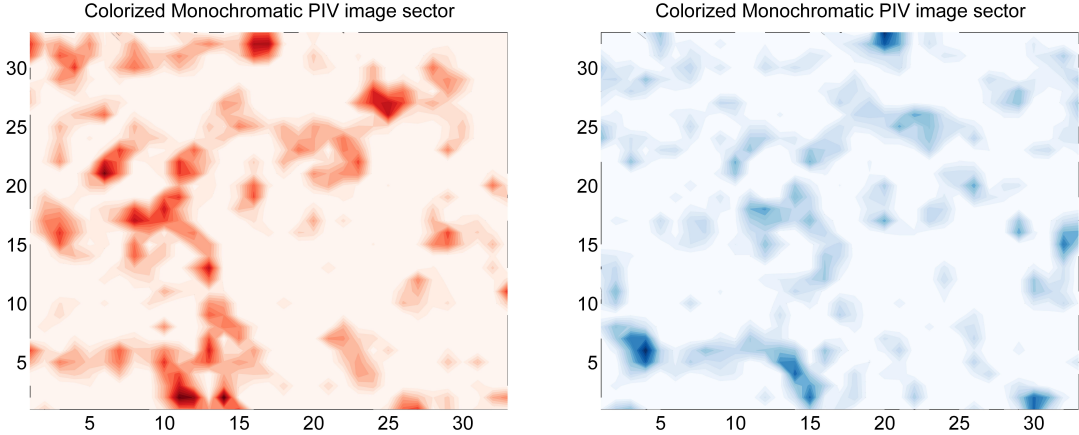


**Figure 8:** Colorized 32x32 pixel contour images at  $t = 0$  (left), and  $t = dt$  (right), no up sampling.

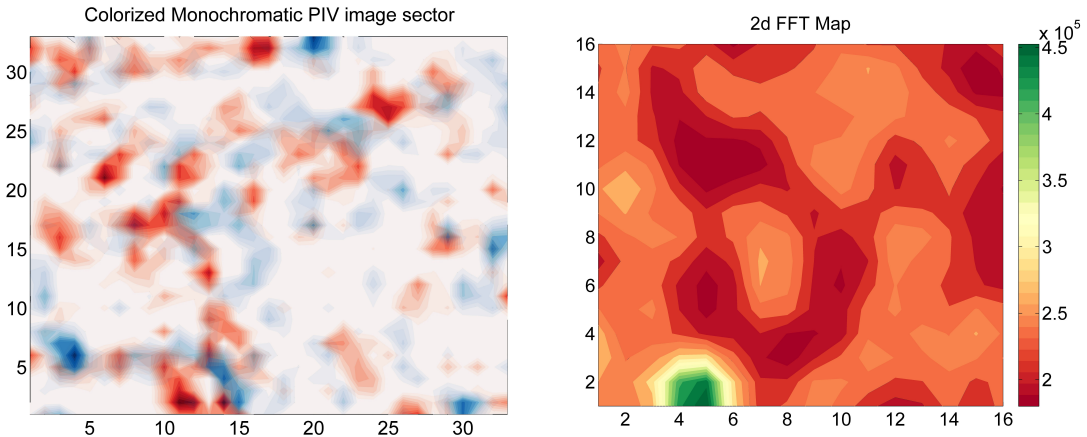


**Figure 9:** Overlaid sector snapshots (left) and corresponding correlation map (right), no up sampling.

Every up sampling doubles the dimensions of the sector, quadrupling the number of pixels and increasing the sub-pixel resolution by a factor of two. The same set of figures is repeated for the same image with 6th order bilinear up sampling in figures 10 and 11. Note that the images are much smoother, and the images have been sampled sufficiently to make a very finely spaced grid. It is important to note

that while bilinear up sampling is used for this example, any other two dimensional method such as cubic may be used.

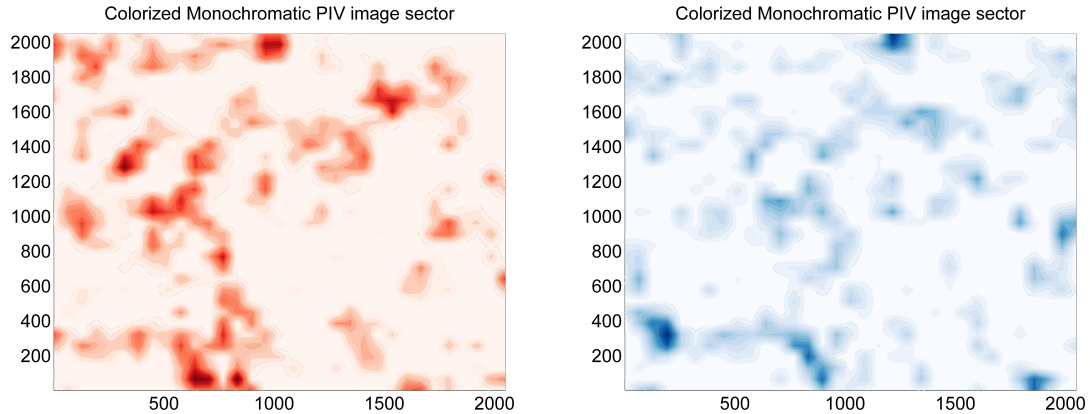


**Figure 10:** Colorized 32x32 pixel contour images at  $t = 0$  (left), and  $t = dt$  (right), 6th order up sampling.

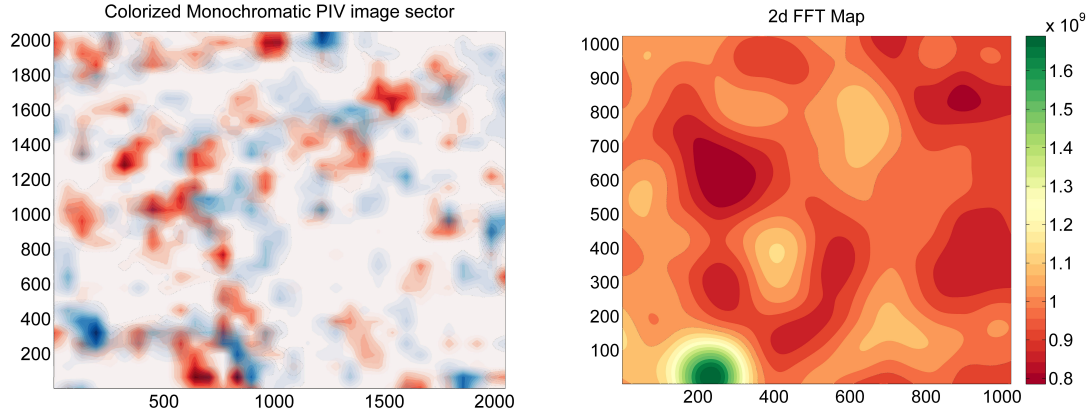


**Figure 11:** Overlaid sector snapshots (left) and corresponding correlation map (right), 6th order up sampling.

As the sampling method creates a finer mesh, the sub-pixel resolution increases. Table 2 shows how the displacement error may vary with sampling order.

Order	$x_{disp}$	$y_{disp}$
0	4	0
1	3.5	0.5
2	3.75	0.25
3	3.625	0.25
4	3.625	0.3125
5	3.625	0.3125
6	3.6406	0.2969
7	3.6406	0.2969

**Table 2:** Pixel displacements by up sampling order.

While the above analysis demonstrates the mathematical motivation behind up sampling images before performing a Fourier transform for measuring particle displacement, it does not adequately describe the total uncertainty in measurements made with particle image velocimetry. The uncertainty associated with measurements made with PIV are dependent upon the geometry of the specific optical setup used to take the data.

### 2.3.2 SEEDING THE FLOW

Appropriate particle seeding density and time between straddled frames is the subject of continued study, and is difficult to predict before hand. Completeness of a two dimensional vector field is highly dependent upon uniform optimal particle density conditions which are difficult to obtain, and maintain over an extended test. For stereo PIV, incomplete data in either of the two dimensional vector sets from either camera at a given spatial location will result in an indeterminate vector

displacement in the three dimensional vector data. To elevate the likelihood that a displacement vector at a given location can be properly determined, an additional data refining technique outlined in Hart (flag, reference) was employed. The Hart method compares correlation maps between two adjacent sectors for consistency. In instances where two adjacent regions lack a well-defined peak, the Hart method functions to magnify shared peaks and reveal a solution that might otherwise have been missed. In instances where sub optimal seeding conditions were present and a correlation map produces a false peak, the Hart method functions to rule the peak out as an anomaly if the adjacent sectors do not also indicate a high correlation at that location. The way in which the Hart method reduces the number of erroneous vectors present in a data set is difficult to quantify on a case by case basis, but any impact on overall uncertainty of the PIV measurements is expected to have a reducing effect.

## 2.4 STEREO PIV DATA ACQUISITION

The low speed wind tunnel was outfitted with a stereo particle image velocimetry system (PIV) capable of resolving three dimensional velocity vector fields within the interrogation plane. Two cameras were mounted with a simple frame built from 80mmx120mm T-slot extruded aluminum with six sliding fastener points on the exterior of the wind tunnel, just outside the test section on the left and right sides as shown in figure 12.

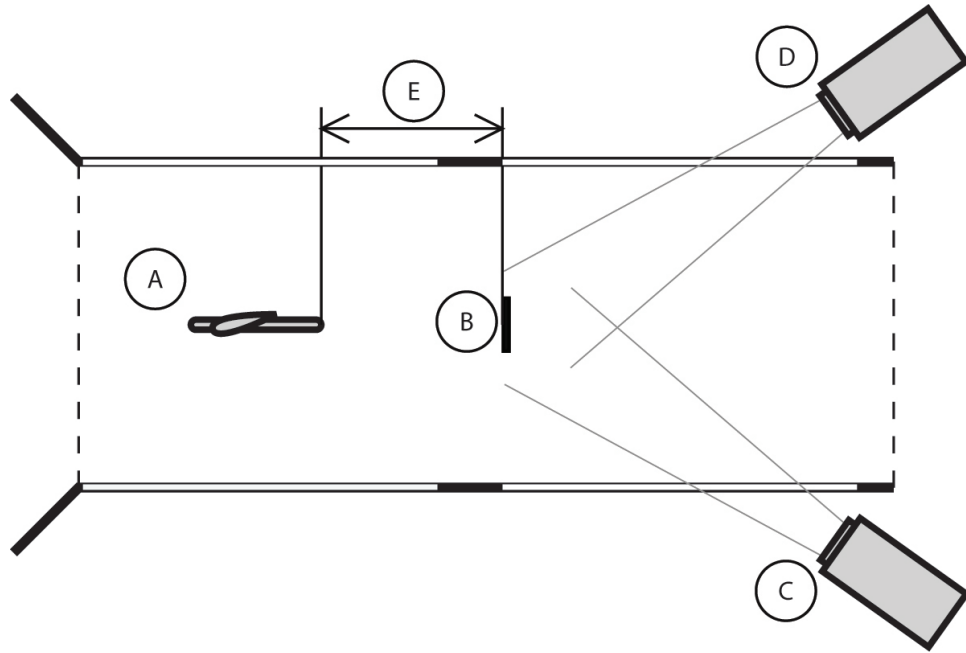


**Figure 12:** Top view schematic of PIV camera positions. A-vortex generator, B-PIV calibration target and interrogation plane, C-left camera, D-right camera, E-station distance dimension.

Each of these cameras was capable of independently resolving a two-dimensional velocity field. An Nd:YAG laser was attached to the roof of the wind tunnel, just outside of a glass window and pointed downwards to illuminate a cross section of the fluid flow perpendicular to the free stream velocity vector as shown in Figure 13. In this image, the fluid flow has been freshly seeded near the vortex generator and a vortex structure is clearly defined with a visible vortex core. In this figure, the bright lines mark the edges of the light curtain.

The equipment used for this study was a "TSI Stereo Image Velocimeter System", which consists of a pair of TSI PIV 13-8 cameras, a TSI synchronizer and frame grabber specific to the cameras, a New Wave Dual Mini-YAG Laser and Light Guide,

a precision 3-D calibration target for stereo PIV camera alignment, and a precision camera and laser traverse system.

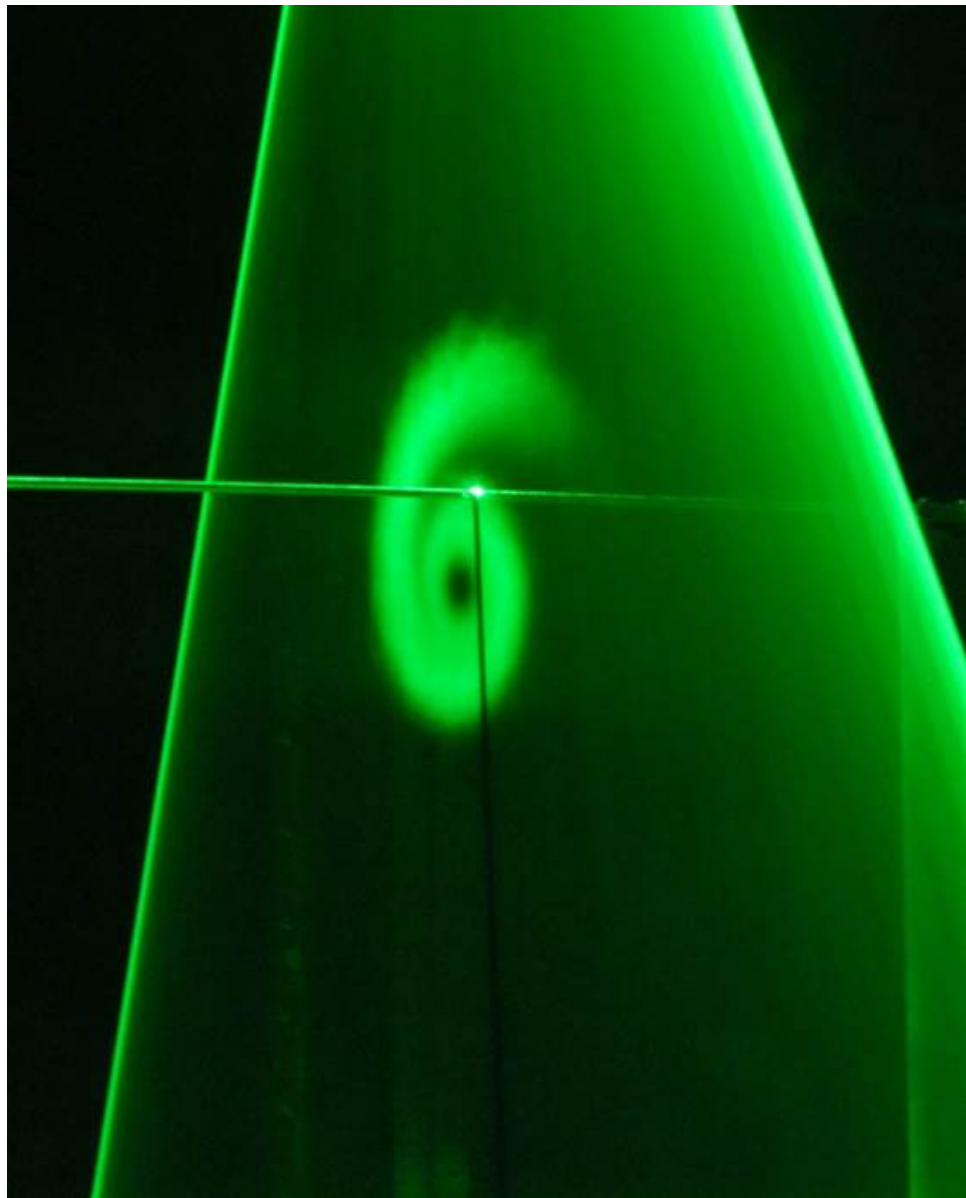


**Figure 13:** Picture of a light curtain illuminating a cross section of an axial wake vortex.

#### 2.4.1 SYNCHRONIZING THE CAMERAS AND LASER

In order to resolve particle displacements on such a small scale in a relatively fast

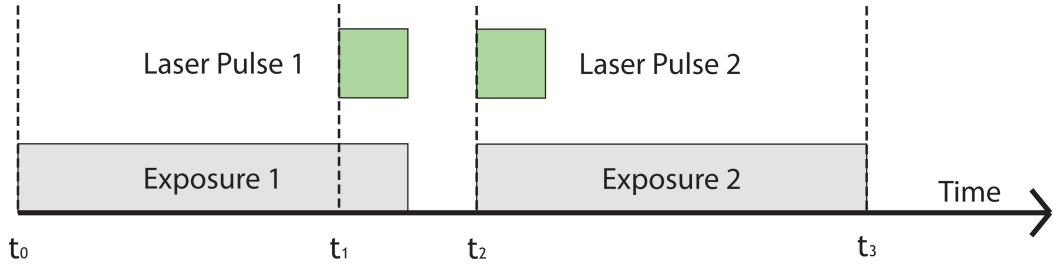


**Figure 14:** Frame straddling technique. Laser pulses are shown in green, and camera exposures are shown in gray.

moving fluid, the time between a pair laser pulses must be tuned to allow sufficient particle displacement occur to obtain a meaningful velocity measurement. If the time interval ( $dT$ ) between successive exposures was too long, the particles escape the interrogation plane, and cannot be tracked to measure their displacement. This study varied the laser pulse timing between 25 microseconds for higher wind tunnel speed, and 50 microseconds for slower vortices associated with slower wind tunnel speed. The cameras used for these experiments however could not support an exposure time on the order of microseconds, consequently a frame straddling technique was used. Frame straddling initiates the first shutter opening well before the first laser pulse begins such that the camera shutter first closes at as the first laser pulse is ending, but before the second laser pulse starts. The second exposure begins just as the second laser pulse is initiating, though it extends well beyond the termination of the first laser pulse as shown schematically in Figure 14.

Timing is achieved by the synchronizer and control PC shown in figure 15. The control PC sends a command to the synchronizer to take an image sample, then the synchronizer sends precisely timed signals to both cameras and the laser control unit.

The cameras each store the image pair in an internal memory buffer before returning the data to the control PC.

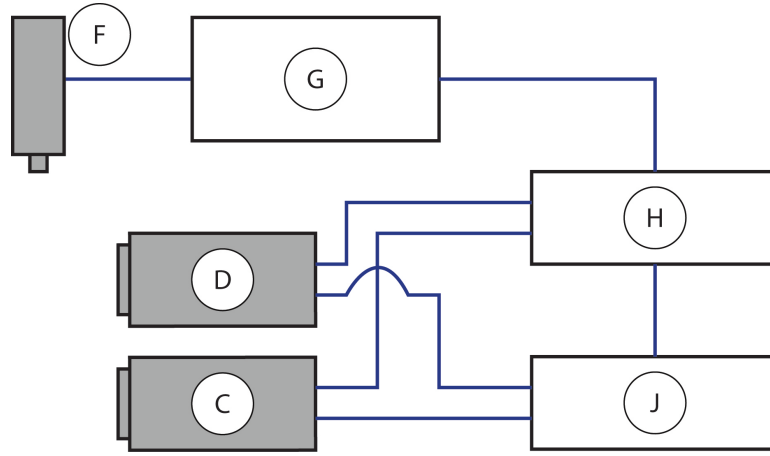


**Figure 15:** Blockdiagram of PIV hardware components. C-left camera, D-right camera, F-Nd:YAG laser, G-laser control unit and power supply, H-synchronizer, J-control PC running INSIGHT software suite.

#### 2.4.2 CALIBRATION EMPLOYING A PIV TARGET

Dimensional calibration is accomplished with the use of a calibration target, a  $10\text{cm}$  by  $10\text{cm}$  black calibration target with precisely positioned white divots and a center fiducial mark ,as shown in figure 16. The calibration target is positioned inside the tunnel test section and aligned with the desired interrogation plane. The laser illumination sheet is set to a continuous firing mode and aimed into the test section so that the location of the interrogation sheet is clearly visible with the use of polarized eye protection. The camera facing face of the interrogation target is then manually aligned with the interrogation plane, which is visible as an intense line of light with a nominal thickness of  $1.5\text{mm}$  across the top of the target. Once

the calibration target was properly aligned, the laser and all other light sources in the facility were extinguished and a lamp is placed downstream of the test section (to create ideal lighting conditions) and illuminate the target for camera focusing. Cameras outfitted with 50mm lenses were manually aimed at the calibration target, taking care to place the fiducial mark near the center of the frame. Focusing must also be done manually by adjusting each lens, and a limited PIV data set was taken after focusing to ensure the focus is sharp enough to resolve a partially complete velocity vector field within the interrogation plane.

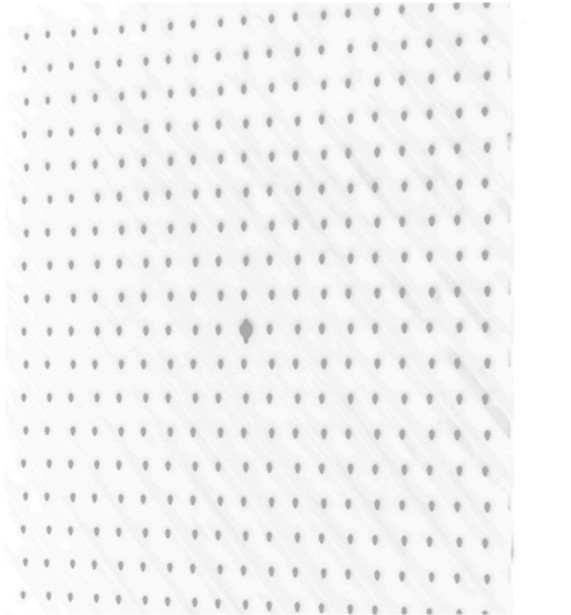


**Figure 16:** Inverted color and elevated contrast photograph of the calibration target, highlighting the central fiducial mark.

INSIGHT software was used to take snapshots and view them to ensure proper focus and alignment. Once satisfactory adjustments were obtained, calibration images were taken and the imaging software was used to recognize the fiducial mark,

as well as each divot, in order to create a two dimensional coordinate transform map that relates pixel distance to physical distance. This calibration was used both in determining the magnitudes of the two dimensional vector fields unique to each camera, and aligning the two separate vector fields, in order to create a three dimensional velocity field. Once calibration images have been acquired, the target was removed from the tunnel and data were taken over a range of velocities in that interrogation plane. Each interrogation plane is defined by its position downstream relative to the trailing edge of the vortex generator. Several interrogation planes were required, and every time it was changed, it was necessary to repeat the calibration process. Ideally, as dictated by good design of experiments practice, the order of experiments should be randomized. This, however, would have required exclusive tunnel use for a longer period of time than could be scheduled due to the level of demand at the time.

#### **2.4.3 SEEDING THE FLOW**

Gathering data with a PIV system requires the flow be properly seeded with particles. Particles should be sufficiently small to be entrained in the flow such that particle motion and fluid motion are the same. The low speed wind tunnel uses mineral oil fog as seed. The density of particle seed which produces the most complete PIV data set depends upon the free stream velocity and the spacing between velocity vector measurements. Each velocity measurement requires a sector of pixels through which displacement can be tracked. If a majority of particles are allowed to travel outside of a given sector between consecutive frame straddled image captures, a meaningful correlation map cannot be generated. Care is taken to ensure particles

travel no more than 50% of a sector width during the time interval between images by adjusting the time between image captures ( $dt$ ). Utilization of a 50% border when processing each sector, as described in the previous section, helps to ensure particles do not escape the interrogation area. A sufficient quantity of particle groups must be visible in each sector to yield a meaningful correlation map. If the particle seed density is too low, or too high, it will result in a more homogeneous image, with more ambiguous and peaks in the correlation map, which results in more spurious data with a poor signal to noise ratio. Manipulation of sector size can increase the number of particles and the reliability of the correlation mapping, but only at the expense of velocity field resolution, as more pixels are required to resolve each vector.

#### 2.4.4 PRESSURE MEASUREMENTS

Pressure measurements within the vortex core could assist in demonstrating the applicability of pressure relaxation phenomenon in describing the behavior of an axial wave vortex, especially combined with simultaneous three-dimensional turbulence measurements with PIV [?]. Initially, it was believed that a pressure probe could be positioned inside the flow within the vortex core. Without positioning the probe in many locations across the flow and post-processing the data set, it was necessary to have some other way to verify that the pressure probe was in fact positioned within the vortex core. Simultaneous PIV and pressure measurements were attempted with a seven hole probe, but the probe and probe mounting system was found to severely obstruct the PIV laser sheet and camera views, and created bright reflections that saturated image values in the vicinity of the vortex. No usable PIV

data could be taken while a pressure probe was mounted in the tunnel test section. Furthermore, upon direct visual inspection of the live vortex core employing a continuous laser sheet, the core appeared to dilate significantly in the presence of the pressure probe. Without a method to compensate for this potential core dilation, pressure measurements of the vortex core region could not be included in the final experiments of this study. It is possible that, with a much larger vortex core which is less sensitive to the presence of a pressure probe, a special non-reflective coating on the pressure probe, and forward mounted PIV cameras looking downrange, simultaneous vortex core pressure measurements and PIV measurements could be obtained. a much larger vortex, forward mounted PIV cameras looking downrange, and a special coated non-reflective pressure probe could allow simultaneous vortex core pressure and PIV measurements.

#### **2.4.5 CAPTURING PIV IMAGERY**

The experiments were conducted with the interrogation plane at seven downstream locations between 546mm and 1016mm. Each of these downstream locations will be referred to as a "station". Tests were conducted starting nearest to the vortex generator and progressing downstream. Since changing the position of the interrogation plane required a complete re-calibration of the PIV system, the testing sequence was not randomized. For each station, data were taken for each of the ten test velocities between 15m/s and 33m/s in ascending order, gaining speed over time. Image pairs were acquired once per second, at a rate of 1Hz for a period of 200 seconds, generating a total of 200 image sets. Each test set of images was then processed

using INSIGHT software in order to produce text files containing three-dimensional vector fields for each image set.

Tunnel conditions were monitored closely and recorded for the duration of each test. Ancillary wet bulb and dry bulb temperatures were taken with a sling psychrometer. The amount of mineral oil fog (seed) was not controllable in a quantitative manner over an extended period of testing, because the dissipation rate was not constant. Additional fog was added to the tunnel through a hose in the tunnel wall, far upstream of the high speed test section, on a qualitative basis. Prior to actual PIV data acquisition, a few test PIV images were captured, and a low quality two dimensional computation was performed real time for a heads-up evaluation of data quality. On occasion, low data quality indicated a low particle density in the tunnel, so additional particle fog was added. Specific details for each test including the relative humidity ( $\phi$ ) derived from wet bulb and dry bulb measurements and associated pressure relaxation coefficient ( $\eta_P$ ), are summarized in Tables 3 through 9.

Stations are defined by the position of the interrogation plane, measured downstream from the wing edge of the bi-wing vortex generator, expressed as  $I_Z$ . Nominal velocity is denoted by  $V_{nom}$ , while actual mean free stream velocity is denoted by  $V_{fs}$ , and variance in the measurement for the duration of the test is labeled  $\sigma_{V_{fs}}$ . Dynamic pressure is  $Q$ , atmospheric pressure is  $P_{atm}$ , and the tunnel temperature is  $T_{tunnel}$ . Relative humidity  $\phi$  was calculated from wet bulb and dry bulb temperatures ( $T_w$  and  $T$ , respectively) by equations 6 through 9 according to [?]. Finally, pressure

relaxation coefficient is calculated as in equation ?? by [?].

$$e_S = 6.112 \exp\left(\frac{17.67T}{T + 243.5}\right) \quad (6)$$

$$e_W = 6.112 \exp\left(\frac{17.67T_W}{T_W + 243.5}\right) \quad (7)$$

$$e = e_W - P_{atm}(T - T_W)0.00066(1 + (0.00115T_W)) \quad (8)$$

$$\phi = 100 \frac{e}{e_S} \quad (9)$$

Run <i>ID</i>	$I_Z$ (mm)	$V_{nom}$ (m/s)	$dt$ ( $\mu$ s)	$V_{fs}$ (m/s)	$\sigma_{V_{fs}}$ (m/s)	$Q$ (Pa)	$P_{atm}$ (Pa)	$T_{tunnel}$ (°K)	$\phi$ (%)	$\eta_P$ ( $\mu$ s)
1	546	15	50	15.22	0.02	135	102036	299.85	60.4	0.35
2	546	17	50	16.88	0.02	170	102115	297.55	66.3	0.329
3	546	19	50	19.43	0.01	225	102105	297.55	66.3	0.329
4	546	21	50	21.06	0.02	264	102100	297.75	66.3	0.324
5	546	23	35	23.21	0.04	321	102097	297.95	66.3	0.324
6	546	25	35	24.86	0.05	371	102093	298.15	66.3	0.324
7	546	27	35	27.02	0.03	434	102092	298.3	66.3	0.324
8	546	29	25	29.12	0.04	505	102080	298.35	66.3	0.324
9	546	31	25	30.86	0.06	564	102050	299.15	66.3	0.324
10	546	33	25	32.98	0.05	641	102054	299.9	60.4	0.35

**Table 3:** Experimental measurements for station 1

Run	$I_Z$	$V_{nom}$	$dt$	$V_{fs}$	$\sigma_{V_{fs}}$	$Q$	$P_{atm}$	$T_{tunnel}$	$\phi$	$\eta_P$
$ID$	(in)	(m/s)	( $\mu s$ )	(m/s)	(m/s)	(Pa)	(Pa)	( $^{\circ}K$ )	(%)	( $\mu s$ )
11	708	15	40	15.27	0.02	138	101185	296.05	69.8	0.312
12	708	17	40	16.89	0.02	169	101218	296.55	69.8	0.312
13	708	19	40	19.03	0.02	215	101219	296.55	69.8	0.312
14	708	21	40	21.13	0.02	264	101186	296.85	66.3	0.329
15	708	23	40	23.21	0.04	321	101150	297.85	66.8	0.329
16	708	25	25	25.36	0.04	380	101120	297.45	71.7	0.301
17	708	27	25	27.03	0.03	432	101120	297.75	70.1	0.306
18	708	29	25	29.12	0.06	498	101106	298.55	73.3	0.297
19	708	31	25	30.87	0.04	562	101109	298.95	73.3	0.297
20	708	33	25	33.39	0.04	653	101101	299.65	73.3	0.297

**Table 4:** Experimental measurements for station 2

Run	$I_Z$	$V_{nom}$	$dt$	$V_{fs}$	$\sigma_{V_{fs}}$	$Q$	$P_{atm}$	$T_{tunnel}$	$\phi$	$\eta_P$
$ID$	(in)	(m/s)	( $\mu s$ )	(m/s)	(m/s)	(Pa)	(Pa)	( $^{\circ}K$ )	(%)	( $\mu s$ )
21	787	15	40	15.2	0.02	136	101094	297.95	72	0.295
22	787	17	40	17.27	0.02	176	101100	297.85	72	0.295
23	787	19	40	19.36	0.03	222	101102	297.95	70.2	0.305
24	787	21	40	21.09	0.03	262	101088	297.95	75.3	0.287
25	787	23	40	23.15	0.02	316	101079	298.05	75.3	0.287
26	787	25	25	24.86	0.02	364	101062	298.45	71.9	0.298
27	787	27	25	26.95	0.04	430	101054	298.65	70.2	0.305
28	787	29	25	29.09	0.04	496	101051	299.05	71.9	0.298
29	787	31	25	31.26	0.04	576	101056	299.35	71.9	0.298
30	787	33	25	32.94	0.04	636	101024	299.75	77	0.283

**Table 5:** Experimental measurements for station 3

Run	$I_Z$	$V_{nom}$	$dt$	$V_{fs}$	$\sigma_{V_{fs}}$	$Q$	$P_{atm}$	$T_{tunnel}$	$\phi$	$\eta_P$
$ID$	(in)	(m/s)	( $\mu s$ )	(m/s)	(m/s)	(Pa)	(Pa)	( $^{\circ}K$ )	(%)	( $\mu s$ )
31	863	15	40	14.86	0.02	133	101865	295.75	63.8	0.354
32	863	17	40	17.39	0.02	180	101855	295.95	63.8	0.354
33	863	19	40	19.08	0.02	219	101847	296.1	63.8	0.354
34	863	21	40	21.13	0.05	267	101845	296.15	63.8	0.354
35	863	23	40	23.29	0.02	323	101844	296.45	63.8	0.354
36	863	25	25	24.98	0.05	373	101840	296.65	65.6	0.344
37	863	27	25	27.09	0.05	438	101843	297	65.6	0.344
38	863	29	25	28.81	0.03	493	101848	297.55	65.6	0.344
39	863	31	25	30.87	0.04	570	101842	298.15	-	-
40	863	33	25	33.44	0.06	661	101844	298.35	-	-

**Table 6:** Experimental measurements for station 4

Run	$I_Z$	$V_{nom}$	$dt$	$V_{fs}$	$\sigma_{V_{fs}}$	$Q$	$P_{atm}$	$T_{tunnel}$	$\phi$	$\eta_P$
$ID$	(in)	(m/s)	( $\mu s$ )	(m/s)	(m/s)	(Pa)	(Pa)	( $^{\circ}K$ )	(%)	( $\mu s$ )
41	914	15	40	14.88	0.02	132	101815	296.25	57.5	0.386
42	914	17	40	17.24	0.03	180	101812	296.35	55.8	0.398
43	914	19	40	19.08	0.03	217	101812	294.45	55.8	0.398
44	914	21	40	21.18	0.03	267	101816	296.65	55.8	0.398
45	914	23	40	23.24	0.03	323	101809	296.95	55.8	0.398
46	914	25	25	24.9	0.03	371	101802	297.15	55.8	0.398
47	914	27	25	27.08	0.04	435	101788	297.45	55.8	0.398
48	914	29	25	29.19	0.03	506	101784	297.85	55.8	0.398
49	914	31	25	31.28	0.05	584	101786	298.15	56.1	0.393
50	914	33	25	33.05	0.05	645	101789	298.75	56.1	0.393

**Table 7:** Experimental measurements for station 5

Run	$I_Z$	$V_{nom}$	$dt$	$V_{fs}$	$\sigma_{V_{fs}}$	$Q$	$P_{atm}$	$T_{tunnel}$	$\phi$	$\eta_P$
<i>ID</i>	(in)	(m/s)	( $\mu s$ )	(m/s)	(m/s)	(Pa)	(Pa)	( $^{\circ}K$ )	(%)	( $\mu s$ )
51	965	15	40	15.31	0.02	140	102039	294.85	61.2	0.381
52	965	17	40	17.36	0.03	182	102034	294.95	61.2	0.381
53	965	19	40	19.08	0.03	219	102035	295.15	59.5	0.392
54	965	21	40	21.23	0.03	270	102037	295.35	59.5	0.392
55	965	23	40	23.33	0.03	327	102018	295.65	59.5	0.392
56	965	25	25	24.97	0.03	375	102021	295.95	59.5	0.392
57	965	27	25	27.05	0.06	437	102008	297.85	52.6	0.422
58	965	29	25	29.17	0.04	505	102005	298.15	47.4	0.454
59	965	31	25	30.9	0.06	571	102015	297.85	53.7	0.421
60	965	33	25	33.04	0.06	653	102009	297.35	53.7	0.421

**Table 8:** Experimental measurements for station 6

Run	$I_Z$	$V_{nom}$	$dt$	$V_{fs}$	$\sigma_{V_{fs}}$	$Q$	$P_{atm}$	$T_{tunnel}$	$\phi$	$\eta_P$
<i>ID</i>	(in)	(m/s)	( $\mu s$ )	(m/s)	(m/s)	(Pa)	(Pa)	( $^{\circ}K$ )	(%)	( $\mu s$ )
61	1016	15	40	15.31	0.03	140	101977	296.15	52	0.434
62	1016	17	40	16.98	0.04	171	101969	296.25	52	0.434
63	1016	19	40	19.1	0.03	218	101961	296.3	52	0.434
64	1016	21	40	21.15	0.05	269	101950	296.45	49.4	0.45
65	1016	23	25	23.23	0.05	321	101953	296.77	52.6	0.422
66	1016	25	25	24.96	0.05	371	101951	297.07	52.6	0.422
67	1016	27	25	27.05	0.5	436	101936	297.25	52.6	0.422
68	1016	29	25	29.17	0.03	505	101928	297.76	52.6	0.422
69	1016	31	25	31.31	0.05	581	101921	297.85	52.6	0.422
70	1016	33	25	33.01	0.05	647	101922	298.3	52.6	0.422

**Table 9:** Experimental measurements for station 7

## 2.5 STEREO PIV DATA PROCESSING

Raw PIV data was processed into text files containing lists of vectors and positions from raw image data with commercial INSIGHT software. This format is considered to be the starting point for the present analysis. Each vector is recorded as a row in a "v3d" file, with a set of position coordinates, velocity vector components, and two quality control flags that were used to reduce spurious vector count. An example of this data is shown in Table 10.

X mm	Y mm	Z mm	U m/s	V m/s	W m/s	CHC	Residual Pixels
8.02046	0.174553	0	0.415872	-2.25951	13.5873	1	0.127058
9.74656	0.174553	0	0.386507	-2.4523	13.9244	1	0.166965
11.4727	0.174553	0	1.01919	-2.8773	14.9454	1	0.0480147
13.1988	0.174553	0	1.30872	-3.02836	15.2081	1	0.0560525

**Table 10:** Example rows from v3d files with raw 3d vector data

The position coordinates are expressed in units of millimeters from the fiducial mark on the target used for calibration. These coordinates are expressed from the viewpoint of the cameras, which were pointed upstream; positive  $X$  coordinates are to the right, positive  $Y$  is upwards, and positive  $Z$  is towards the cameras. Vector components are recorded as  $U$ ,  $V$  and  $W$ .

### 2.5.1 REYNOLDS AVERAGING

Since each run contained 200 separate vector sets, this data needed to be synthesized into values that compare well with the Reynolds Averaged Navier Stokes equations in cylindrical coordinates. This processing was performed in Python 2.7 and Matlab, with much of the code entirely replicated in each language. First, text

files with tables of vector data were loaded into a parser to construct a mesh grid of the  $X$ ,  $Y$  coordinate space. These mesh grids establish the relationship between matrix indices and real coordinate space with units of  $mm$ . Then, for each test as shown in Table 1, data from each of the 200 snapshots is Reynolds averaged to produce a stable velocity component, and a fluctuating velocity component in each dimension for each vector, as expressed in equation 10 in terms of position  $x$  at time  $t$ .

$$u(x, t) = \bar{u}(x) + u'(x, t) \quad (10)$$

Each component is given an individual variable name, with stable nonfluctuating components taken from a simple average of all sets expressed as the component letter with an over bar ( $\bar{u}$ ,  $\bar{v}$ ,  $\bar{w}$ ), and time averaged fluctuating component expressed with a prime ( $\bar{u}'$ ,  $\bar{v}'$ ,  $\bar{w}'$ ). Velocities referring to just one of the 200 sets will use a subscript  $i$  as ( $u_i$ ,  $v_i$ ,  $w_i$ ). The stable components are computed with a simple average to preserve the sign, while the fluctuating components are computed with a root mean squared method as shown in equations 11 through 16.

$$\bar{u} = \frac{1}{N} \sum_{i=1}^{200} u_i \quad (11)$$

$$\bar{v} = \frac{1}{N} \sum_{i=1}^{200} v_i \quad (12)$$

$$\bar{w} = \frac{1}{N} \sum_{i=1}^{200} w_i \quad (13)$$

$$\bar{u}' = \sqrt{\frac{1}{N-1} \sum_{i=1}^{200} (u_i - \bar{u})^2} \quad (14)$$

$$\bar{v}' = \sqrt{\frac{1}{N-1} \sum_{i=1}^{200} (v_i - \bar{v})^2} \quad (15)$$

$$\bar{w}' = \sqrt{\frac{1}{N-1} \sum_{i=1}^{200} (w_i - \bar{w})^2} \quad (16)$$

Where  $\bar{u}$ ,  $\bar{v}$  and  $\bar{w}$  are the time averaged velocity components in the  $X$ ,  $Y$ ,  $Z$  directions respectively, and  $\bar{u}'$ ,  $\bar{v}'$  and  $\bar{w}'$  are the time averaged fluctuating velocity components.

Similarly, time averaged Reynolds stresses can be calculated by multiplying the fluctuating components together before taking the root mean square average by equations 17 through 22.

$$\bar{u}'\bar{u}' = \sqrt{\frac{1}{N-1} \sum_{i=1}^{200} ((u_i - \bar{u})(u_i - \bar{u}))^2} \quad (17)$$

$$\bar{v}'\bar{v}' = \sqrt{\frac{1}{N-1} \sum_{i=1}^{200} ((v_i - \bar{v})(v_i - \bar{v}))^2} \quad (18)$$

$$\bar{w}'\bar{w}' = \sqrt{\frac{1}{N-1} \sum_{i=1}^{200} ((w_i - \bar{w})(w_i - \bar{w}))^2} \quad (19)$$

$$\bar{u}'\bar{v}' = \sqrt{\frac{1}{N-1} \sum_{i=1}^{200} ((u_i - \bar{u})(v_i - \bar{v}))^2} \quad (20)$$

$$\overline{u'w'} = \sqrt{\frac{1}{N-1} \sum_{i=1}^{200} ((u_i - \bar{u})(w_i - \bar{w}))^2} \quad (21)$$

$$\overline{v'w'} = \sqrt{\frac{1}{N-1} \sum_{i=1}^{200} ((v_i - \bar{v})(w_i - \bar{w}))^2} \quad (22)$$

Turbulent kinetic energy  $k$  can be calculated as one half of the sum of the three double correlation components as in equation 23.

$$k = \frac{1}{2} (\overline{u'u'}^2 + \overline{v'v'}^2 + \overline{w'w'}^2) \quad (23)$$

Once all the statistics for Cartesian coordinates have been generated, the vortex core must be found in order to convert all values to cylindrical coordinates. The core is found by finding the minimum in-plane velocity magnitudes near the center of the interrogation plane, excluding the stream wise  $w$  component. In practice, to avoid confusion in identifying the vortex core due to spurious edge values, a threshold value is defined that limits the search for in-plane velocity minima to an area near the center of the field of view. Once the lowest value was found, sub-grid accuracy was achieved by taking a cubic interpolation of the grid points surrounding the minimum. This technique was sufficiently robust to automatically identify the core correctly in every test.

With a location for the vortex core, new mesh grids in radial and tangential coordinates,  $R$  and  $\theta$ , are created from the  $X$  and  $Y$  mesh grids. Velocity components,  $r$  and  $t$ , are then calculated by equations 24 and 25.

$$r_i = u_i \cos(\theta) + v_i \sin(\theta) \quad (24)$$

$$t_i = u_i \sin(\theta) - v_i \cos(\theta) \quad (25)$$

Where  $r_i$  and  $t_i$  represent a radial and tangential velocity matrix for just one of the 200 total surveys, and  $\theta$  is the mesh grid of angles about the vortex core. These equations were applied on an element wise basis to every grid point in the vector field. Once this was done, the same Reynolds averaging technique was applied to separate the radial and tangential velocity components  $r$  and  $t$  into stable and fluctuating components in equations 26 through 29.

$$\bar{r} = \frac{1}{N} \sum_{i=1}^{200} r_i \quad (26)$$

$$\bar{t} = \frac{1}{N} \sum_{i=1}^{200} t_i \quad (27)$$

$$\bar{r}' = \sqrt{\frac{1}{N-1} \sum_{i=1}^{200} (r_i - \bar{r})^2} \quad (28)$$

$$\bar{t}' = \sqrt{\frac{1}{N-1} \sum_{i=1}^{200} (t_i - \bar{t})^2} \quad (29)$$

The double correlations in cylindrical coordinates were calculated directly from the transformed cylindrical velocities with equations

$$\overline{r'r'} = \sqrt{\frac{1}{N-1} \sum_{i=1}^{200} ((r_i - \bar{r})(r_i - \bar{r}))^2} \quad (30)$$

$$\overline{t't'} = \sqrt{\frac{1}{N-1} \sum_{i=1}^{200} ((t_i - \bar{t})(t_i - \bar{t}))^2} \quad (31)$$

$$\overline{r't'} = \sqrt{\frac{1}{N-1} \sum_{i=1}^{200} ((r_i - \bar{r})(t_i - \bar{t}))^2} \quad (32)$$

$$\overline{r'w'} = \sqrt{\frac{1}{N-1} \sum_{i=1}^{200} ((r_i - \bar{r})(w_i - \bar{w}))^2} \quad (33)$$

$$\overline{t'w'} = \sqrt{\frac{1}{N-1} \sum_{i=1}^{200} ((t_i - \bar{t})(w_i - \bar{w}))^2} \quad (34)$$

Once this processing is complete, we have large set of Reynolds averaged velocity data available for each of the 70 test cases. Plots of this data from test case 55 will be shown as examples. Stream plots can be produced as in figure 17. Cartesian average velocity components for test case is shown in figures 18 through 20, though they are not particularly useful when compared to values in cylindrical coordinates. Cylindrical average velocity components are shown in figures 21 and 22. Reynolds stresses are shown in figures 23 through 25. Turbulent energies are shown in figures 26 through 28. Total turbulent kinetic energy  $k$  is shown in figure 29. Scatter plots that flatten the dataset into one dimension can be generated as in the tangential velocity vs distance to core plot shown in figure 30.

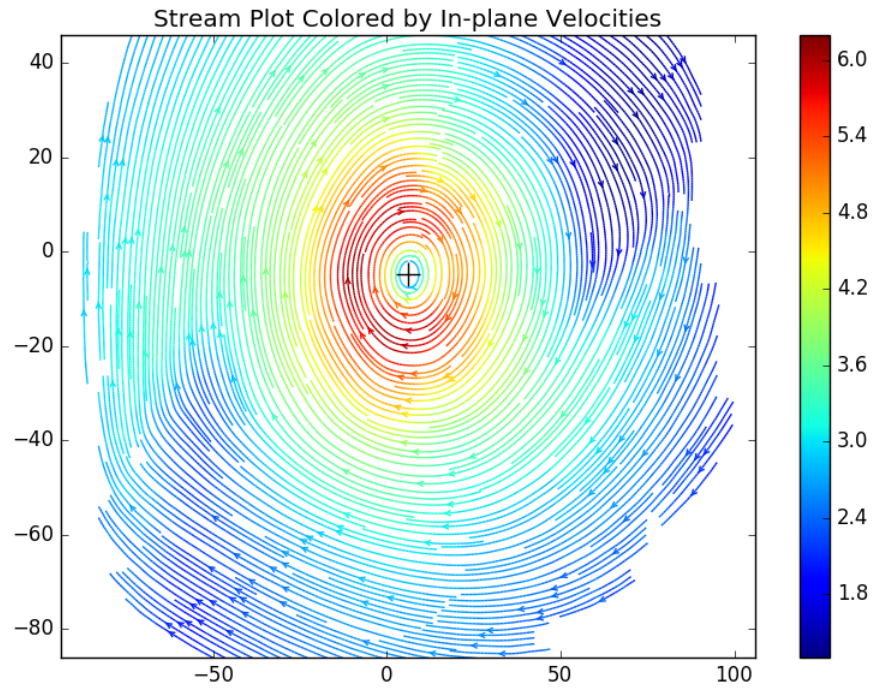


**Figure 17:** Example stream plot.

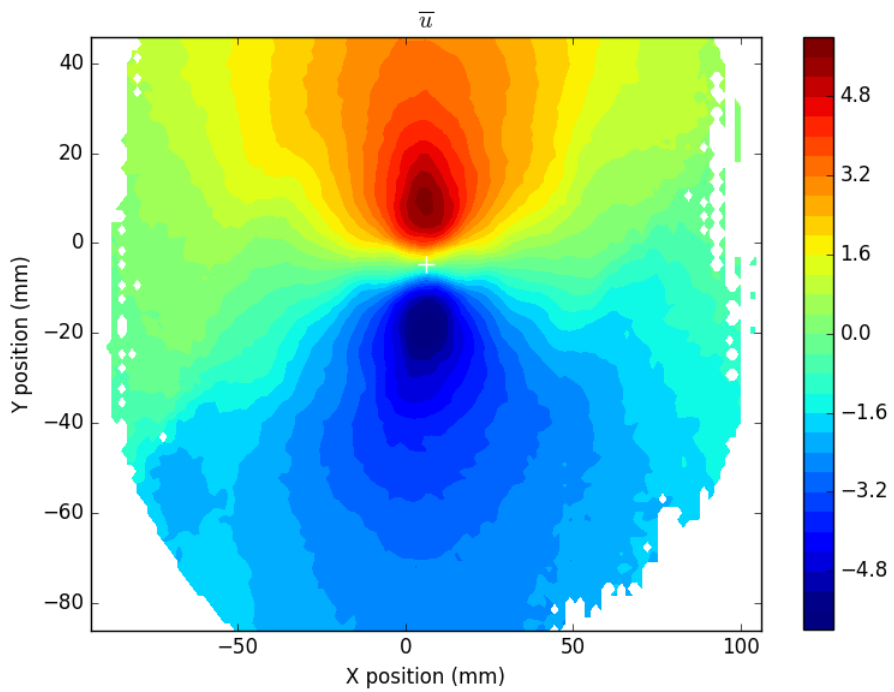


**Figure 18:** Example contour plot of  $\bar{u}$ .

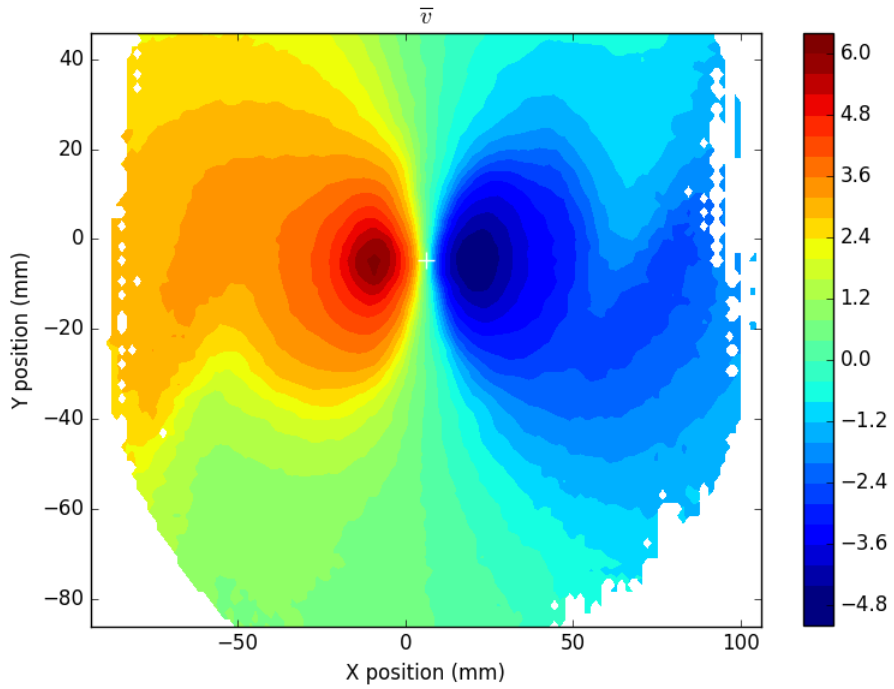


**Figure 19:** Example contour plot of  $\bar{v}$ .

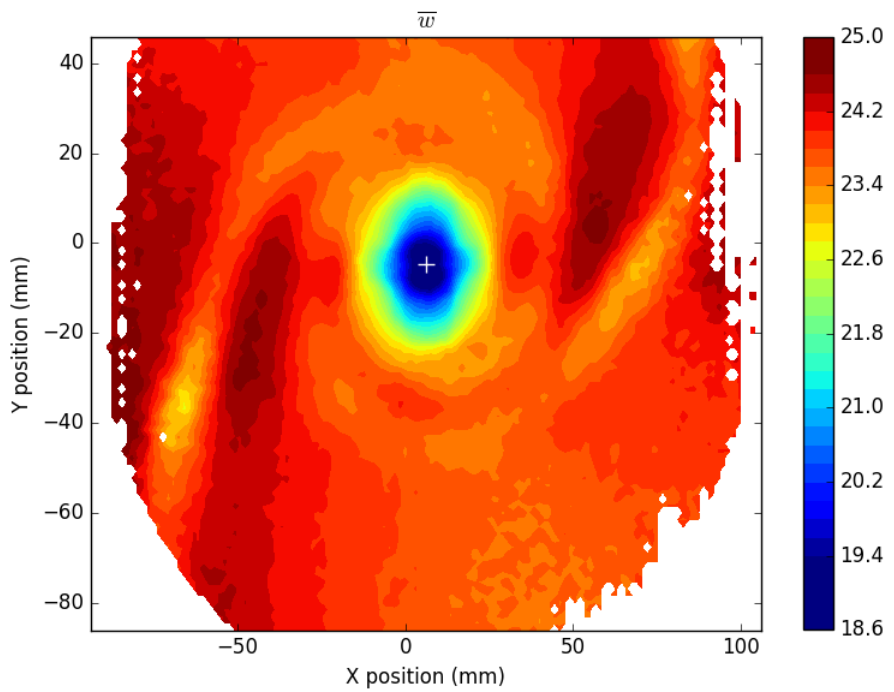


**Figure 20:** Example contour plot of  $\bar{w}$ .

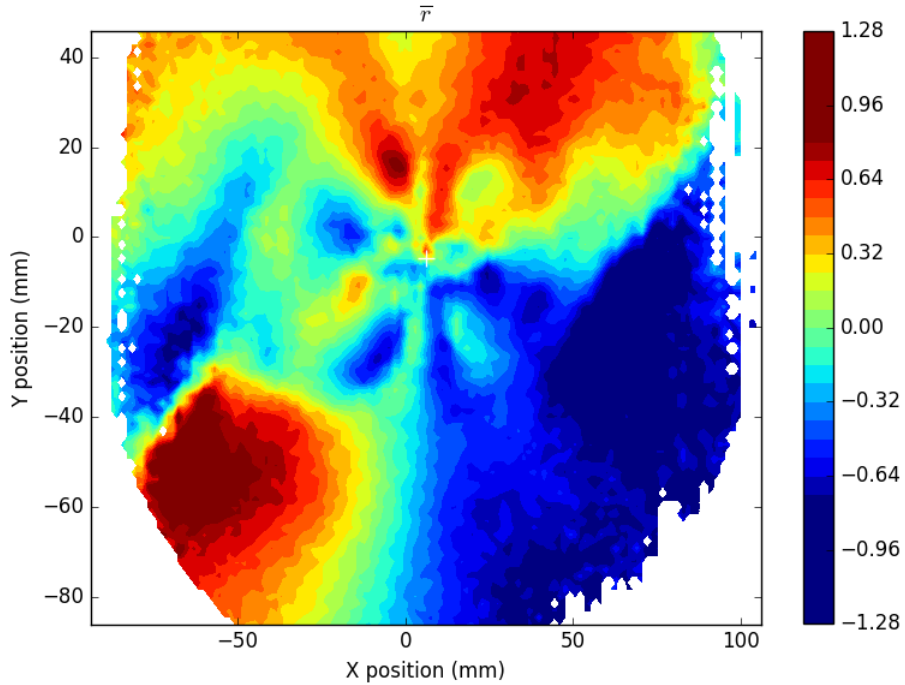


**Figure 21:** Example contour plot of  $\bar{r}$ .

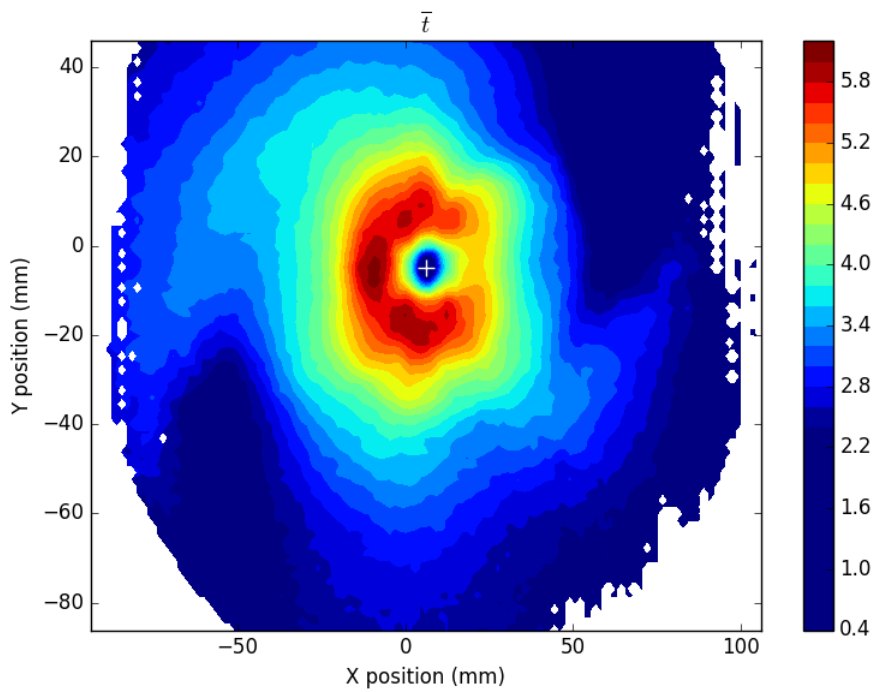


**Figure 22:** Example contour plot of  $\bar{t}$ .

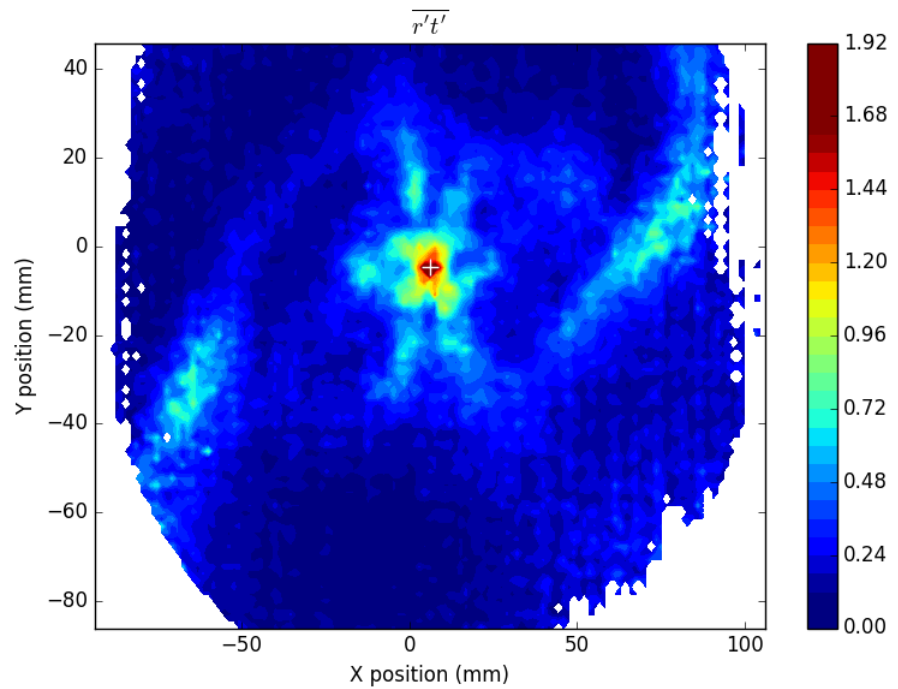


**Figure 23:** Example contour plot of  $\overline{r't'}$ .

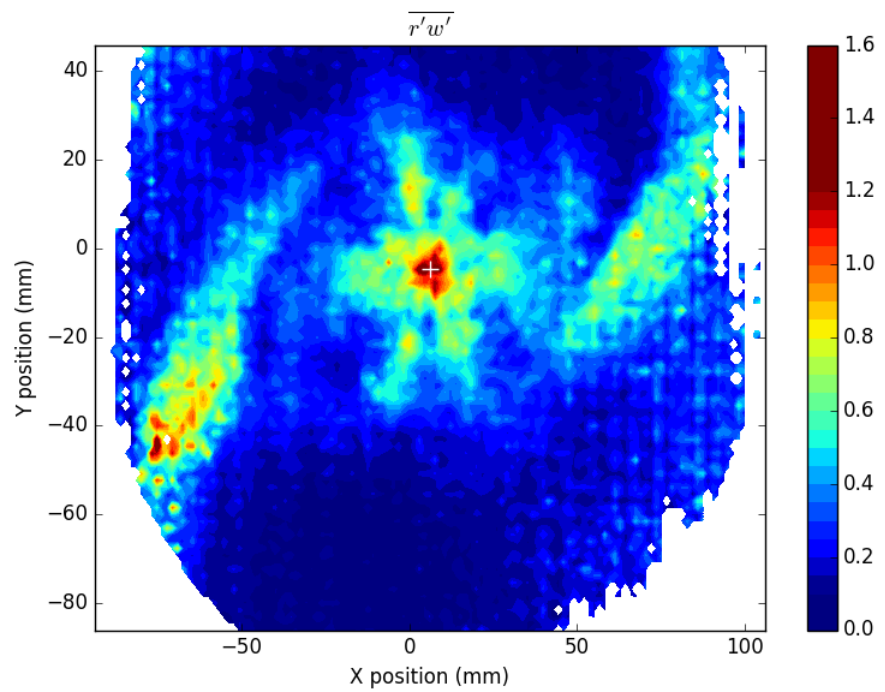


**Figure 24:** Example contour plot of  $\overline{r'w'}$ .

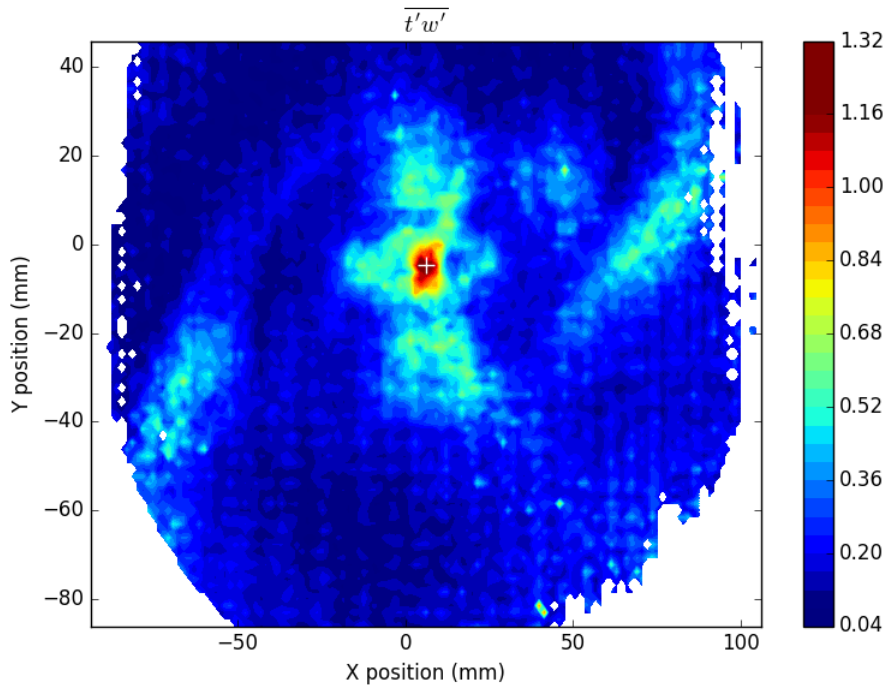


**Figure 25:** Example contour plot of  $\overline{t'w'}$ .

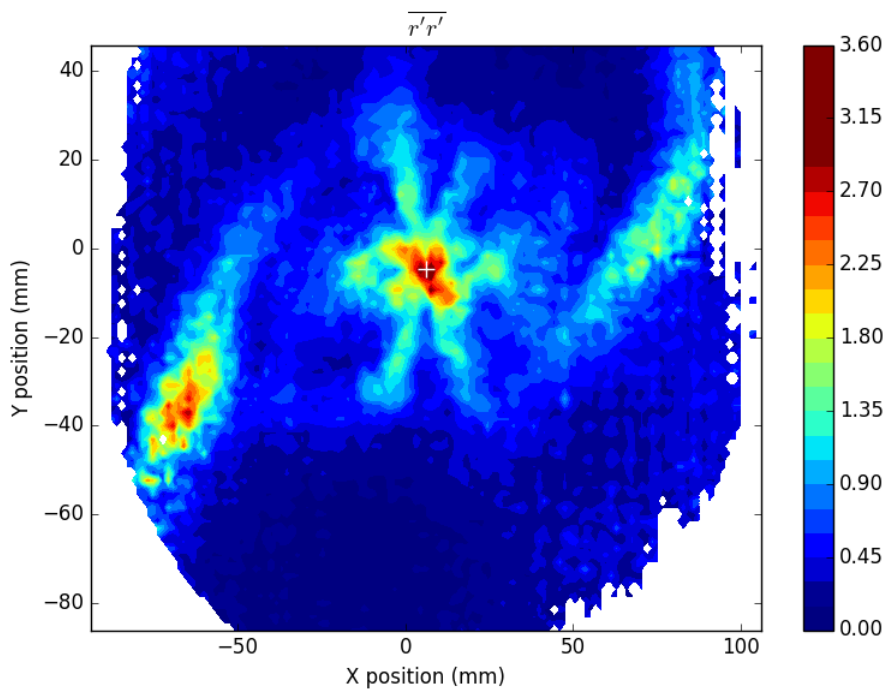


**Figure 26:** Example contour plot of  $\overline{r'r'}$ .

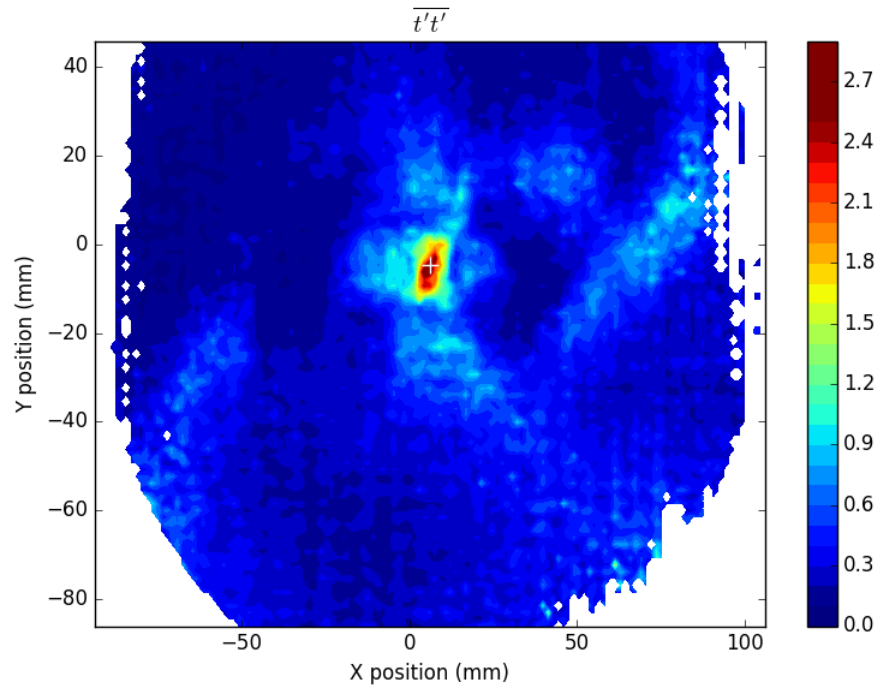


**Figure 27:** Example contour plot of  $\overline{t}t'$ .

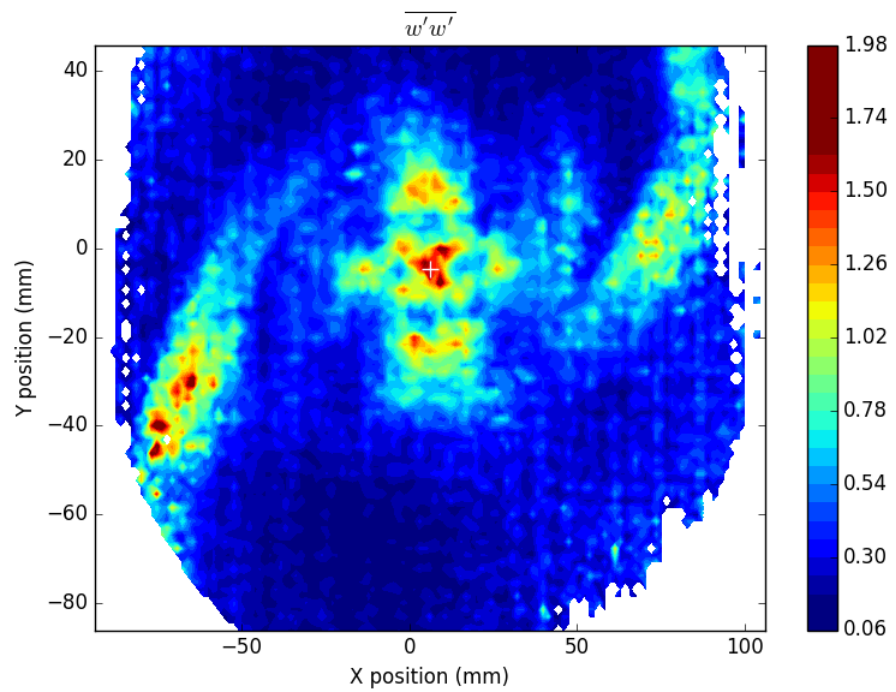


**Figure 28:** Example contour plot of  $\overline{w}'w'$ .

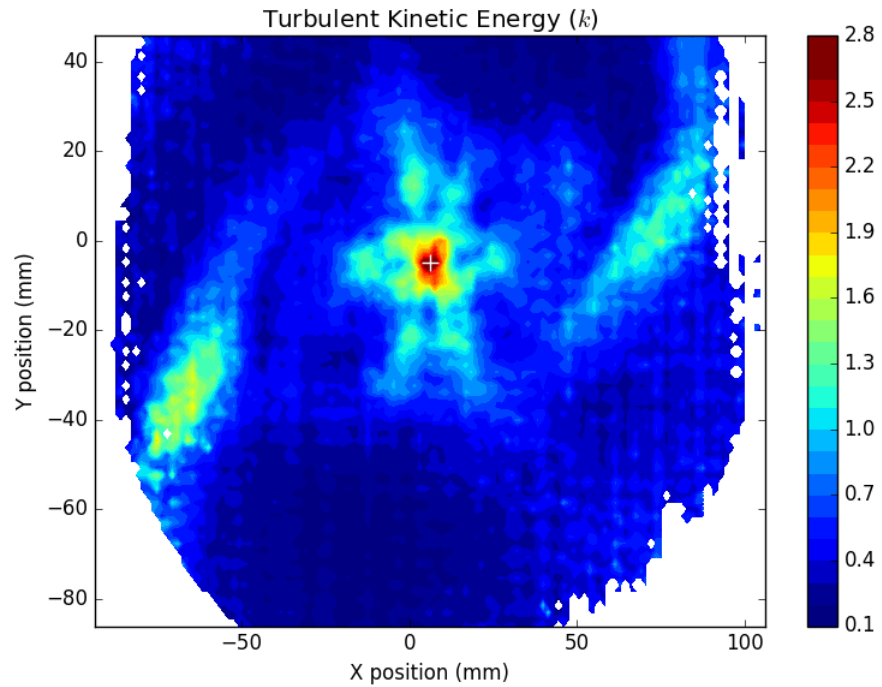


**Figure 29:** Example contour plot of turbulent kinetic energy  $k$ .

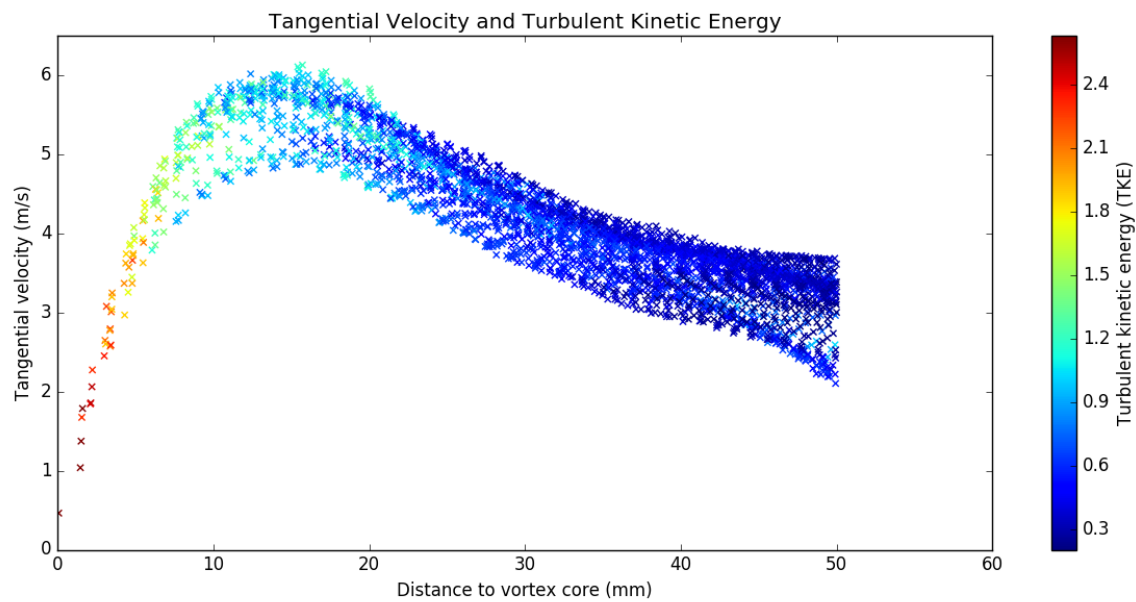


**Figure 30:** Example scatter plot of  $T$ , colored by  $k$ .

Insight to the quality and uncertainty in each measurement was gained by examining the number of vectors successfully extracted from the set of 200 snapshots as shown in Figure 31. Locations with fewer than twenty valid vectors in the set of 200 were thrown out. A clear relationship between the total turbulent kinetic energy,  $k$ , and the number of vectors making up the average was observed, and is discussed in Chapter 3.

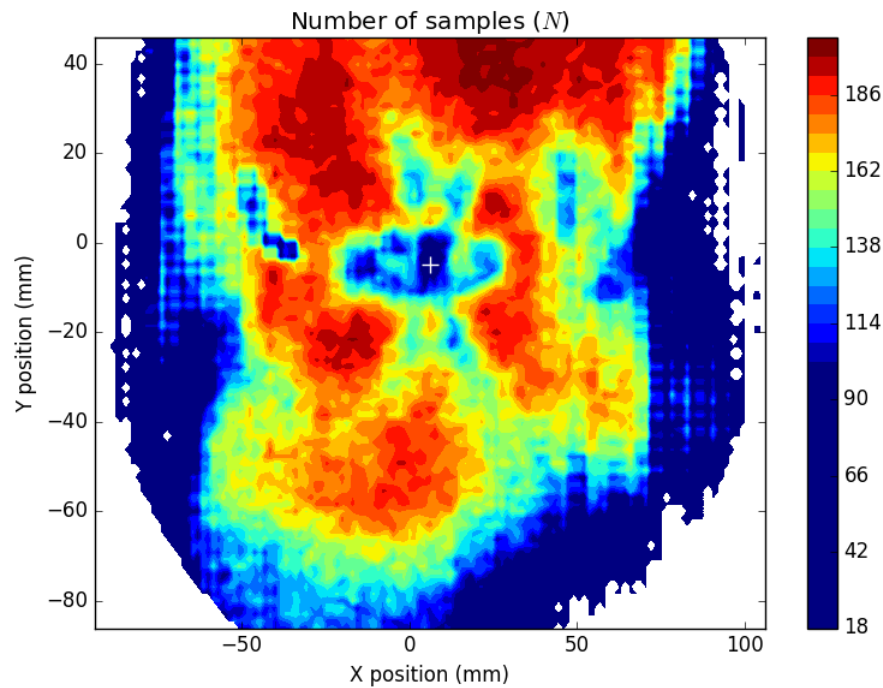


**Figure 31:** Example contour plot showing the variation in the number of measurements within the interrogation plane

## 2.6 UNCERTAINTY IN PIV MEASUREMENTS

There are a number of factors that contribute to uncertainty in PIV measurements. Both bias and precision errors can be estimated by considering detailed

information about the optical geometry of the PIV setup. Monte Carlo based error estimation techniques can be applied by creating artificially simulated images with randomly distributed particles [?]. The distribution of these particles can be modeled using a Gaussian intensity profile by (flag, reference) as described in Equation 35.

$$I(x, y) = I_0 \exp \left( \frac{-(x_{img} - x_p)^2 - (y_{img} - y_p)^2}{\frac{1}{8} d_\tau^2} \right) \quad (35)$$

Where  $x_p$  and  $y_p$  are the locations of the particle centroid,  $d_\tau$  is the diameter of the particle, and  $I_0$  is particle intensity. Particle intensity is directly related to the intensity of the light sheet, which is modeled as a Gaussian distribution [?]. This assumption allows us to express particle intensity as 36

$$I_0(z_p) = (q) \exp \left( -\frac{z_p^2}{\frac{1}{8} \Delta Z_L^2} \right) \quad (36)$$

Where  $z_p$  is the particles position within the thickness of the light sheet,  $q$  is the particle light scattering efficiency, and  $\Delta Z_L$  is the thickness of the light sheet.

These formula are used to generate artificial image pairs for a single camera. A sufficient number of particles are created with  $x$ ,  $y$  and  $z$  coordinates to meet particle density parameters, these coordinates are then used to generate light intensities according to Equation 36, which populate the image plane of the first image  $A$ . Next, a displacement image,  $B$ , is generated by shifting all the particles in a predetermined direction in three dimensional space. It is worth noting that for a single camera setup, particle movements in the  $z$  direction do not produce pixel displacements, but simply determine the intensity of the light reflected from the particle. The known

particle displacements can then be compared against outputs calculated with PIV capture and processing software.

To translate this concept to stereo PIV, an additional step is required. Instead of directly placing particles with known coordinates onto the image plane of one camera, they are placed on a conceptual version of the interrogation plane. The coordinate transforms obtained from PIV calibration are used to map the displacements from the conceptual plane into the image plane of each camera. These coordinate transforms are unique to each camera, and depend upon the optical geometry of the PIV setup. Uncertainty is calculated using the recommended AIAA calibration procedure outlined in [?]. To determine the system bias, the mean difference between the velocity standard established by the Monte Carlo simulation and the velocity calculated by the PIV software are compared as follows

$$\overline{\Delta U} = \frac{1}{N} \left( \sum_{i=1}^N \Delta U_i \right), \quad (37)$$

$$\overline{\Delta V} = \frac{1}{N} \left( \sum_{i=1}^N \Delta V_i \right), \quad (38)$$

$$\overline{\Delta W} = \frac{1}{N} \left( \sum_{i=1}^N \Delta W_i \right) \quad (39)$$

Which is simply the average difference between the known velocity components and the measured velocity components  $\Delta U$ ,  $\Delta V$ , and  $\Delta W$  for a large number of simulations. This is referred to as the bias, and the three bias components are denoted as

$$\beta_U = \overline{\Delta U} \quad (40)$$

$$\beta_V = \overline{\Delta V} \quad (41)$$

$$\beta_W = \overline{\Delta W} \quad (42)$$

The measurement precision is reported as the root-mean-square of the standard deviation, calculated as in

$$S_{\Delta U} = \sqrt{\frac{1}{N-1} \left( \sum_{i=1}^N (\Delta U_i - \overline{\Delta U})^2 \right)} \quad (43)$$

$$S_{\Delta V} = \sqrt{\frac{1}{N-1} \left( \sum_{i=1}^N (\Delta V_i - \overline{\Delta V})^2 \right)} \quad (44)$$

$$S_{\Delta W} = \sqrt{\frac{1}{N-1} \left( \sum_{i=1}^N (\Delta W_i - \overline{\Delta W})^2 \right)} \quad (45)$$

Resulting in precision calculations given by

$$P_{\overline{U}} = \frac{2S_{\Delta U}}{\sqrt{N}} \quad (46)$$

$$P_{\overline{V}} = \frac{2S_{\Delta V}}{\sqrt{N}} \quad (47)$$

$$P_{\overline{W}} = \frac{2S_{\Delta W}}{\sqrt{N}} \quad (48)$$

Total uncertainty for each component at the 95% confidence level is calculated by combining the bias and precision via to obtain

$$U_{\overline{\Delta U}} = \sqrt{\beta_U^2 + P_U^2} \quad (49)$$

$$U_{\overline{\Delta V}} = \sqrt{\beta_V^2 + P_V^2} \quad (50)$$

$$U_{\overline{\Delta W}} = \sqrt{\beta_W^2 + P_W^2} \quad (51)$$

For these experiments, artificial pixel displacements were created to emulate the expected range of flow field conditions. These conditions include variance in the streamwise velocity  $W$  between 10 and 40  $m/s$ , and in the spanwise components  $X$ , and  $Y$  of 0 to 10  $m/s$ . The value of 1 was used for  $N$  in the precision Equations 46 through 48. Even though many samples were taken at every vector location, the uncertainty in each individual measurement was of great importance for studying the unstable component of the velocity, and thus turbulent phenomena. The Monte Carlo analysis shows....

(flag, unfinished, need to run new Monte Carlo code)

## Chapter 3

### EXPERIMENT RESULTS

words here

## Bibliography

## VITA

Jeffry William Ely  
Department of Aerospace Engineering  
Old Dominion University  
Norfolk, VA 23529

Bachelors of Mechanical Engineering, Old Dominion University, December 2011